

1 ~~On the S/Z Relationship for Rimed Snow Particles in the W-band~~

2 **W-band S/Z Relationships for Rimed Snow Particles: Observational Evidence from**  
3 **Combined Airborne and Ground-based Observations**

4  
5 Shelby Fuller <sup>1</sup>, Sam Marlow <sup>1</sup>, Samuel Haimov <sup>1</sup>, Matthew Burkhart <sup>1</sup>, Kevin Shaffer <sup>1</sup>, Austin  
6 Morgan <sup>1</sup>, and Jefferson R. Snider <sup>1,2</sup>

7  
8 <sup>1</sup> Department of Atmospheric Science, University of Wyoming, Laramie, WY, USA

9  
10  
11  
12 <sup>2</sup> Corresponding Author, jsnider@uwyo.edu

13

## 14 Abstract

15 Values of ~~undercatch-corrected~~ liquid-equivalent snowfall rate (S) at a ground site and  
16 microwave reflectivity (Z) retrieved using an airborne W-band radar were acquired during  
17 overflights. The temperature at the ground site was between -6 and -15 °C. At flight level, within  
18 clouds containing ice and supercooled liquid water, the temperature was approximately 7 °C  
19 colder. Additionally, airborne measurements of snow particle imagery were acquired. The  
20 images demonstrate that most of the snow particles were rimed, ~~at least a flight level~~. A  
21 relatively small set of S/Z pairs (4) are available from the overflights. Important distinctions  
22 between these measurements and those of Pokharel and Vali (2011), who also reported W-band  
23 S/Z pairs for rimed snow particles, are 1) the fewer number of ~~S/Z data~~-pairs, 2) the method used  
24 to acquire S, and 3) the ~~altitude, relative to ground,~~ ~~altitude~~ of the Z retrievals. This analysis  
25 ~~indicates It also shown that the a computationally-based~~ S/Z relationship ~~reported in Pokharel~~  
26 ~~and Vali (2011) applied in W band retrievals yields an can underestimate~~ S, in scenarios with  
27 snowfall produced by riming, that- is substantially larger than that derived using an S/Z  
28 ~~relationship by developed for unrimed snow particles~~ ~~approximately a factor of two when~~  
29 ~~snowfall is produced by riming.~~

30

## 31 1 - Introduction

32 Improvement of methods used to measure snowfall and rainfall are an ongoing focus of  
33 meteorological research. The various methods are ground-based instruments that evaluate the  
34 mass of precipitation that falls into or onto a collector (precipitation gauges) (Brock and  
35 Richardson 2001), ground-based radars (Wilson and Brandes 1979), and airborne and space-  
36 borne radars (Matrosov 2007; Kulie and Bennartz 2009; Geerts et al. 2010; Skofronick-Jackson  
37 et al. 2017). An objective of these approaches, whether used to make observations independent  
38 of other methods (e.g., Kulie and Bennartz 2009), or as a component of multiple observations  
39 (e.g., Cocks et al. 2016), is estimation of precipitation rate and accumulation.

40 Many studies have investigated using radar for evaluating rainfall (for a review see  
41 Wilson and Brandes 1979). There are two approaches. The first is research, both observational  
42 and computational, that probes the relationship between rainfall rate (R) and radar-measured  
43 values of [range-corrected](#) backscattered microwave power. The latter is commonly reported as an  
44 equivalent radar reflectivity factor ( $Z_e$ ). The second is operational in the sense that precipitation  
45 gauges are used to calibrate measurements acquired using weather surveillance radars.  
46 Complications associated with converting  $Z_e$  to R, or converting a radar reflectivity factor<sup>1</sup> (Z) to  
47 R, can be grouped in four categories: 1) Inaccuracy in quantification of Z, 2) variation of the  
48 R/Z relationship stemming from precipitation processes (e.g., coalescence and break up), 3)  
49 difference between the volume of a radar range gate versus the much smaller volume of  
50 atmosphere sampled as precipitation falls to a gauge, and 4) vertical displacement between a  
51 radar range gate and a calibrating gauge, especially at far ranges.

---

<sup>1</sup> Radars are calibrated to report  $Z_e$  (Smith 1984). Herein, radar reflectivities are reported as  $Z = Z_e$  and as  $\text{dBZ} = 10\log_{10}(Z_e)$ .

52 For situations with snowfall, methods employing either gauge or radar are associated  
53 with complications beyond that incurred in rainfall (Matrosov 2007; Martinaitis et al. 2015;  
54 Cocks et al. 2016). Problems associated with gauge measurements are wind-induced snow  
55 particle undercatch, gauge capping, delayed registration, and blowing snow aliasing as snowfall.  
56 Moreover, in a situation with snow particles most abundant within a radar range gate, compared  
57 to rain drops, and where a measurement of  $Z$  is used to infer  $R$  via a  $R/Z$  relationship, the  
58 resultant precipitation rate will likely be inaccurate. This is because hydrometeor shape, density,  
59 and dielectric properties are all variable for snow particles while relatively invariant for rain  
60 drops. Additionally, a snow particle's terminal fall speed varies with size (as is the case for  
61 drops) and with particle shape and particle density. Going forward, we refer to the latter two  
62 properties as shape and density.

63 The goals of this paper are as follows: 1) to describe measurements of undercatch-  
64 corrected liquid-equivalent snowfall rate ( $S$ ,  $\text{mm h}^{-1}$ ) and how these were paired with W-band  
65 measurements of reflectivity ( $Z$ ,  $\text{mm}^6 \text{m}^{-3}$ ); 2) to contrast the ~~measurement-based~~  $S/Z$  pairs  
66 against ~~calculated~~  $S/Z$  relationships commonly applied in radar retrievals of  ~~$S$ -based-on~~  
67 ~~reflectivity~~; and 3) to investigate why the ~~acquired data set~~  $S/Z$  pairs deviates from predictions of  
68 some ~~calculated~~  $S/Z$  relationships.

69 In calculations of paired values of  $S$  and  $Z$ , density is an important parameter. Density is  
70 commonly estimated using empirical data (e.g., Pokharel and Vali 2011, [PV11]). For graupel, a  
71 snow particle that grows via collection of supercooled cloud droplets in a process commonly  
72 referred to as riming, paired observations of particle mass and particle size have been used to  
73 estimate density. There is considerable uncertainty in this approach. Based on data collected at  
74 two northwestern US surface sites (Zikmunda and Vali 1972; Locatelli and Hobbs 1974), density

75 values differ by at least a factor of two at particle sizes smaller than 2000  $\mu\text{m}$  (PV11; their  
 76 Fig. ~~ure~~ 4). Given that the density of rime ice varies with droplet impact speed, droplet size, and  
 77 temperature (Macklin 1962), it is not surprising that the density-~~versus~~-size relationships  
 78 analyzed by PV11 are so varied.

79 The following introductory paragraphs overview W-band S/Z relationships being applied  
 80 in instances of snowfall where mass is acquired by vapor deposition (crystal), by collection of  
 81 crystals (aggregate), and by riming (rimed crystals and graupel). Henceforth, the latter two snow  
 82 particle types are collectively referred to as rimed snow particles.

83 In a computational study, Hiley et al. (2011) considered a variety of snow particle types  
 84 (column, plate, bullet rosette, sector plate, dendrite, and aggregate), employed a parameterized  
 85 ice particle size distribution (PSD) function (Field et al. 2005), accounted for a range of  
 86 temperature (-5 to -15  $^{\circ}\text{C}$ ) via the Field et al. parameterization, and developed a range of S/Z  
 87 relationships for snow particles. Except for the aggregates, the modeled particle types were  
 88 ~~vapor-grown~~ crystals. Hiley et al.'s upper- and lower-limit relationships are  $S = 0.21 \cdot Z^{0.77}$  and  $S$   
 89  $= 0.024 \cdot Z^{0.91}$ . Matrosov (2007) developed ~~a range of an~~ S/Z relationships for aggregates. In that  
 90 work, ~~parameterized~~ PSDs from Braham (1990) were employed, and a range of particle aspect  
 91 ratios ~~and densities~~ were factored into the calculations. For aggregates, the S/Z relationship is  $S$   
 92  $= 0.056 \cdot Z^{1.25}$  ~~and the upper- and lower-limit S/Z relationships are  $S = 0.11 \cdot Z^{1.25}$  and  $S =$~~   
 93  ~~$0.041 \cdot Z^{1.25}$~~  (Matrosov 2007). It should be noted that Hiley et al. (2011) and Matrosov (2007)  
 94 employed similar, but not identical, computational methods ~~and parameterized mass-size~~  
 95 ~~relationships~~. Kulie and Bennartz (2009) developed an S/Z relationship for what they referred to  
 96 as a "snow particle" type. The wavelength-dependent density derived by Surussavadee and  
 97 Staelin (2007) ( $200 \text{ kg m}^{-3}$  at  $\lambda = 3.2 \text{ mm}$ ) was adopted, the snow particles were modeled as

98 spheres, and the Field et al. parameterization was applied. The S/Z relationship developed for  
99 this particle type is  $S = 0.52 \cdot Z^{0.83}$  (Surussavadee and Staelin 2007; Kulie and Bennartz 2009;  
100 henceforth SSKB). Variance in the calculations discussed in this paragraph originate from  
101 changes in density, shape, fall speed, ~~and~~ PSD, and particle size as these changes are propagated  
102 through the cloud-microphysical and microwave-scattering calculations.

103 ~~In a hybrid approach (computational and an analysis of airborne observations), PV11~~  
104 ~~concluded that most of the snow particles they imaged were rimed snow particles. Their~~  
105 ~~calculations of S and Z, conducted using two density-size relationships (indicated with  $\rho_1$  and~~  
106  ~~$\rho_3$ ), were presented. They compared their calculated reflectivities to measurements of Z from a~~  
107 ~~W band radar. That led to their conclusion that “...the lower density assumption...yielded closer~~  
108 ~~correspondence to observed reflectivities.” Their recommendation for S as a function of Z—~~  
109 ~~hereafter the  $S(\rho_1)/Z$  best fit line—is  $S = 0.39 \cdot Z^{0.58}$ . In addition to variance in their values of S,~~  
110 ~~coming from a dependence on density, PV11 state that a value of S derived via their best-fit line~~  
111 ~~is uncertain by a factor of ten. That uncertainty is evident in the variance seen about the line in~~  
112 ~~Fig. 11 of PV11. Those investigators, and Geerts et al. (2010), attributed the variance to use of~~  
113 ~~two-dimensional snow particle imagery in calculations of S and to actual variations of density~~  
114 ~~and shape not accounted for in the calculations.~~

115 In a hybrid approach (computational and an analysis of airborne observations), PV11  
116 concluded that most of the snow particles they imaged were rimed snow particles. Values of S  
117 were calculated using a density-size function ( $\rho_1$ , discussed below), a fall speed-size function, a  
118 measured PSD and measured particle images, and a determination of particle volumes. It was  
119 assumed that a prolate spheroid approximated particle shape and this was the basis for  
120 determining a particle's sphere-equivalent volume and the particle's sphere-equivalent size. The

121 sphere-equivalent size was applied in the two functions. Values of  $Z$  were calculated using a  
122 measured PSD, sphere-equivalent sizes, the  $\rho_1$  function, and Mie Theory. PV11 presented  
123 calculations of  $Z$ , obtained using two density-size relationships (their Eqs. 1 and 2) and compared  
124 their calculated reflectivities to measurements of  $Z$  from a W-band radar. That led to their  
125 conclusion that “...the lower density assumption...yielded closer correspondence to observed  
126 reflectivities.” Their recommendation for  $S$  as a function of measured  $Z$  - hereafter the  $S(\rho_1)/Z$   
127 best-fit line - is  $S = 0.39 \cdot Z^{0.58}$ . Values of  $Z$  that were paired with the calculated values of  $S$  (i.e.,  
128 the  $S/Z$  pairs from PV11 that we present in Sect. 4), and that were used to determine the  $S(\rho_1)/Z$   
129 best-fit line, came from the WCR. In addition to variance in their values of  $S$ , coming from a  
130 dependence on density, PV11 state that a value of  $S$  derived via their best-fit line is uncertain by  
131 a factor-of-ten. That uncertainty is evident in the variance of  $S/Z$  data pairs about the  $S(\rho_1)/Z$  line  
132 in Fig. 11 of PV11. Those investigators, and Geerts et al. (2010), attributed the variance to use of  
133 two-dimensional snow particle images in calculations of  $S$  and to actual variations of density,  
134 shape, and particle size not accounted for in the calculations.

135 Also relevant are  $S/Z$  relationships reported by Falconi et al. (2018; their Table 2). These  
136 were developed using measurements from a video disdrometer, weighing precipitation gauge,  
137 microwave radiometer, and a vertically-pointing W-band radar. All these systems were operated  
138 at the ground. The data set was stratified into intervals of lightly-rimed, moderately-rimed, and  
139 heavily-rimed snow. A proxy for snow particle riming - radiometer measurements of liquid water  
140 path - was the basis for the stratifications (von Lerber et al. 2017). The  $S/Z$  relationships are  $S =$   
141  $0.10 \cdot Z^{1.0}$  (lightly-rimed),  $S = 0.079 \cdot Z^{1.3}$  (moderately-rimed), and  $S = 0.060 \cdot Z^{1.4}$  (heavily-rimed).

142 Our focus is on surface measurements of  $S$  and on pairing of those measurements with  
143 airborne measurements of  $Z$ . We also analyze airborne measurements of snow particle imagery.

144 The latter demonstrates that the particles observed at flight level were rimed. These  
145 measurements are the basis for our assertion that our data set is relevant to ongoing  
146 investigations of using  $Z$  to evaluate  $S$  in situations where precipitation is produced by riming.

147 Section 2 describes the setting of our study, the instruments we deployed, and recordings  
148 we obtained using two data acquisition systems. One of the data systems was operated at a  
149 ground site and the other on an aircraft. Section 3 is an analysis of the recordings; this section  
150 also considers recordings from two additional, but ancillary, ground sites. Our findings are  
151 discussed in Sect. 4 and summarized in Sect. 5. An Appendix (Sect. 6) explains how we  
152 averaged recordings of near-surface W-band reflectivities and surface-based recordings of  
153 snowfall.



## 154 2 - Site, Aircraft, and Instruments

### 155 2.1 - Site

156 ~~A~~We analyzed herein are aircraft and ground data from 14/15 December 2016, ~~when the~~  
157 ~~analyzed snowfall event spanned a UTC date change,~~ and from 3 January 2017. The ground data  
158 were acquired in a forest/prairie ecotone on the eastern slope of the ~~-~~Medicine Bow Mountains in  
159 southeastern ~~ern~~ Wyoming (Figs. 1a-b). No ground-based observers were deployed during the two  
160 snowfall events ~~we~~ analyzed.

161 At one of three ground sites (HP in Figs. 1a-b) ~~we deployed~~ a hotplate precipitation  
162 gauge (Rasmussen et al. 2011; Zelasko et al. 2018), a GPS receiver, and a data acquisition  
163 system ~~were~~ deployed. Once per second, the data system ingested a hotplate-generated data  
164 string, combined that with time-of-day from the GPS receiver [~~(~~Coordinated Universal Time  
165 (UTC)~~)]~~, and recorded the merged hotplate/UTC data string. The absolute accuracy of the time  
166 stamp is no worse than 2 s.

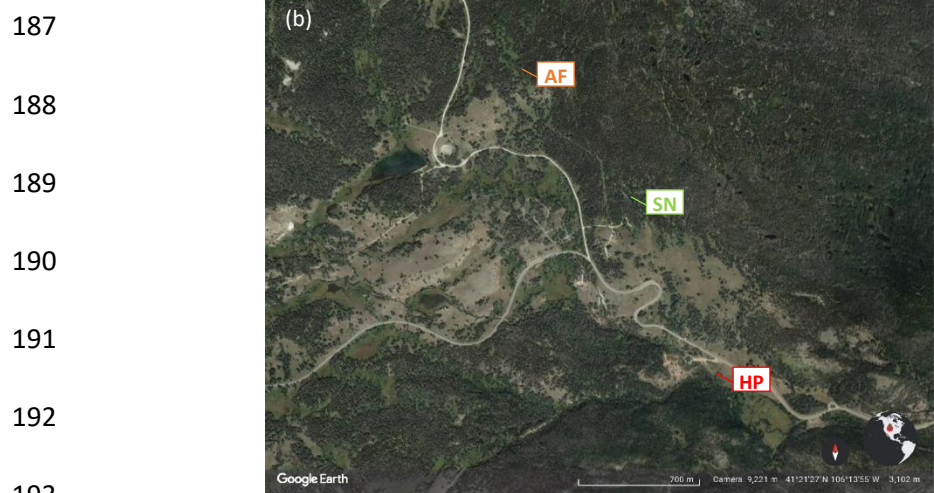
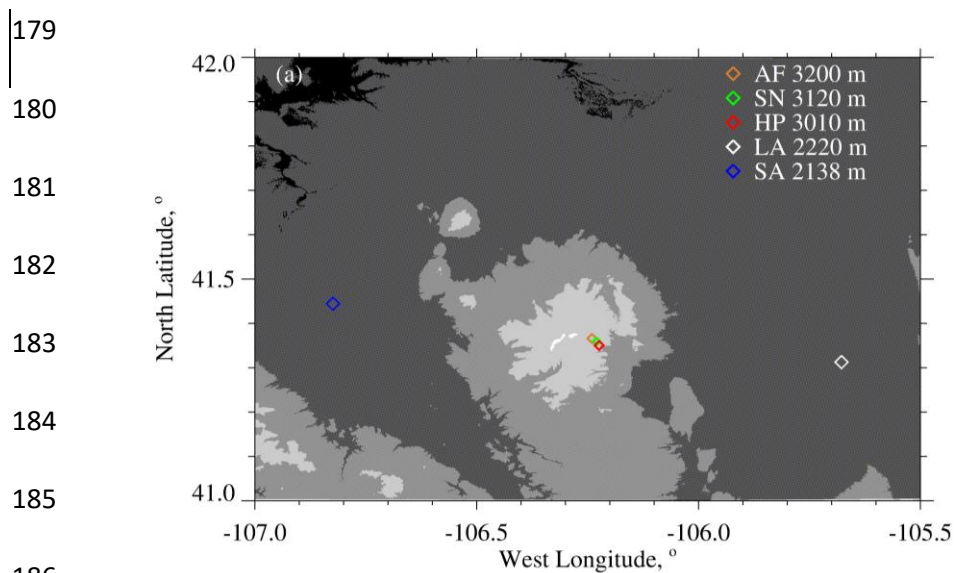
167 Overflights of the hotplate were done by the University of Wyoming King Air (WKA) on  
168 14/15 December 2016 and on 3 January 2017. The flights were conducted in preparation for the  
169 SNOWIE field project (Tessendorf et al. 2019) and were flown from the Laramie, WY Airport  
170 (“LA” in Fig. 1a).

171 Data acquisition on the WKA was also synchronized with UTC, but with much better  
172 accuracy than at the hotplate.

173

174           Measurements of horizontal wind (speed and direction), temperature, relative humidity,  
175 and pressure from the US-GLE AmeriFlux tower (AF in Figs. 1a-b) are also components ~~of~~  
176 ~~the~~ analysis. The AmeriFlux data were provided to us as 30-minute averages (AmeriFlux 2021;  
177 Marlow et al. 2023).

178



195 Figure 1 – (a) Southeast Wyoming, airport at Saratoga, WY (SA), airport at Laramie, WY (LA),  
 196 and the ground sites: AF = US-GLE AmeriFlux tower, SN = Brooklyn Lake SNOTEL, and HP =  
 197 hotplate. Altitudes of the airports and ground sites are in the legend. Altitude thresholds for the  
 198 digital elevation map are 1500, 2000, 2500, 3000, and 3500 meters. (b) Close up of the AF, SN,  
 199 and HP ground sites (from © Google Earth).

200

## 201 2.2 - University of Wyoming King Air (WKA)

202 The following WKA measurements were analyzed: aircraft position, temperature, snow  
203 particle imagery, and three moments of the cloud droplet size distribution function. A Cloud  
204 Droplet Probe (CDP; Faber et al. 2018) was the basis for the droplet size distribution  
205 measurements and the derived moments. The latter are droplet concentration (N), cloud liquid  
206 water content (LWC), and mean droplet diameter ( $\langle D \rangle$ ). Snow particle imagery was obtained  
207 using a precipitation particle imaging probe (2DP; Korolev et al. 2011) and a cloud particle  
208 imaging probe (2DS; Lawson et al. 2006). These acquired two-dimensional images of particles  
209 between 200 to 6400  $\mu\text{m}$  (2DP) and between 10 to 1280  $\mu\text{m}$  (2DS).

## 210 2.3 – The W-band Wyoming Cloud Radar (WCR)

211 Retrievals from the up-looking and down-looking antennas of the WCR, operated on the  
212 WKA, were also analyzed. For this we used Level 2 WCR data<sup>2</sup> with reflectivities recorded as  
213  $dBZ = 10 \cdot \log_{10}(Z)$ . The reflectivities were converted from dBZ to Z prior to processing.  
214 Additionally, values of the vertical-component Doppler velocity retrieved from below the WKA  
215 using the WCR's down-looking antenna were analyzed. The Doppler velocities were corrected  
216 for aircraft motion, as described in Haimov and Rodi (2013). We use  $V_D$  to symbolize the  
217 corrected vertical-component Doppler velocity and adopt the convention that  $V_D > 0$  indicates  
218 upward hydrometeor motion.

219

---

<sup>2</sup> [http://flights.uwyo.edu/uwka/wcr/projects/snowie17/PROCESSED\\_DATA/](http://flights.uwyo.edu/uwka/wcr/projects/snowie17/PROCESSED_DATA/)

220 The Level 2 WCR sampling was different on the two flight days and this difference is  
221 ~~indicated~~shown in Table 1. ~~The flights were conducted in preparation for the SNOWIE field~~  
222 ~~project (Tessendorf et al. 2019) and were flown from the Laramie, WY Airport (“LA” in Fig.~~  
223 ~~1a).~~

224 Ground-based calibrations of the WCR’s up-looking antenna and correlations between in-  
225 flight retrievals acquired using the WCR’s up-looking and down-looking antennas were used to  
226 estimate the ~~precision and~~ absolute accuracy of the WCR-derived values of dBZ. ~~These are  $\pm 1.0$~~   
227 ~~is is~~ dBZ and  $\pm 2.5$  dBZ, respectively (PV11).

228

229 Table 1 – Level 2 WCR sampling and the WKA overflight time

230

Date	Level 2 WCR Vertical Sampling, m	Level 2 WCR Along-track Sampling, s	Overflight Time, UTC
14/15 December 2016	23	0.23	00:00:38 (15 December 2016)
3 January 2017	30	0.36	20:32:03

231

232

## 233 2.4 - Hotplate Gauge

234 Algorithms used to process hotplate measurements are described in Rasmussen et al.  
235 (2011), Boudala et al. (2014), and Zelasko et al. (2018). Henceforth, these are referred to as R11,  
236 B14, and Z18, respectively. This section describes how hotplate measurements acquired at the  
237 HP site were analyzed. The hotplate deployed at the HP site is described in Wolfe and Snider  
238 (2012), Z18, and in Marlow et al. (2023).

239 ~~Four measurements fundamental to the steady state energy budget of the hotplate's~~  
240 ~~temperature-controlled up-viewing plate are output by the hotplate microprocessor as one-minute~~  
241 ~~running averages (Z18). These averages were merged with the GPS time and recorded at 1-Hz by~~  
242 ~~the data acquisition system (Sect. 2.1). The four measurements are electrical power supplied to~~  
243 ~~the plate, ambient temperature, wind speed, and solar irradiance. With these measurements,~~  
244 ~~calibration data (Marlow et al. 2023), and the algorithm developed by Z18, we calculated a~~  
245 ~~liquid-equivalent snowfall rate. The latter was not corrected for snow particle undercatch;~~  
246 ~~however, in what follows we describe that correction.~~

247 ~~Marlow et al. (2023; their Figure 4b) report the relationship between snow particle catch~~  
248 ~~efficiency and wind speed that we applied in calculations of the undercatch-corrected liquid-~~  
249 ~~equivalent snowfall rate. There are three bases for this relationship. First is the catch efficiencies~~  
250 ~~R11 derived using measurements obtained from a weighing gauge, operated within a double~~  
251 ~~fence intercomparison reference shield, and collocated measurements from an unshielded~~  
252 ~~hotplate gauge. We symbolize these paired measurements as SRG (shielded reference gauge) and~~  
253 ~~UHG (unshielded hotplate gauge). R11 plotted hotplate catch efficiencies (i.e., UHG/SRG)~~  
254 ~~versus wind speeds measured at 10 m AGL (their Fig. 8). Second is Marlow et al.'s adjustment~~  
255 ~~of R11's 10 m AGL wind speeds to 2 m AGL. The basis for the adjustment is surface boundary~~

256 ~~layer parameters derived for R11's site (Kochendorfer et al. 2018) and an equation from~~  
257 ~~Panofsky and Dutton (1984; their Eq. 6.7). The adjustment was made because the hotplate-~~  
258 ~~derived wind speeds, both here and in Marlow et al. (2023), were acquired at approximately 2 m~~  
259 ~~above the snowpack surface. Third is Marlow et al.'s comparison of SNOTEL-derived snow~~  
260 ~~water equivalent depth changes and hotplate-derived time-integrated accumulations. The time-~~  
261 ~~base for the comparisons was 24 hours. Based on that comparison, which has 57 paired values~~  
262 ~~acquired at the sites labeled HP and SN in Fig. 1, the average fractional absolute relative~~  
263 ~~difference is 0.30. In the Marlow et al. (2023) comparison (their Fig. 9a), at accumulation = 10~~  
264 ~~mm, imprecision associated with the SNOTEL measurement corresponds to a relative error~~  
265 ~~which is 0.24 (Marlow et al. 2023). This indicates that SNOTEL contributed significantly to the~~  
266 ~~previously-mentioned relative difference and especially so for the smaller accumulations in~~  
267 ~~Figure 9a of Marlow et al. (2023). Because of this, we did not limit calculation of the relative~~  
268 ~~difference to a subset of the 57 paired measurements. Based on this assessment of the relative~~  
269 ~~difference, the hotplate precision applied in this analysis was taken to be 0.3.~~

270 Five measurements fundamental to the steady state energy budget of the hotplate's  
271 temperature-controlled up-viewing plate are output by the hotplate microprocessor as one-minute  
272 running averages (Z18). These averages were merged with the GPS time and recorded at 1 Hz by  
273 the data acquisition system (Sect. 2.1). With these measurements, calibration data (Marlow et al.  
274 2023), and the algorithm developed by Z18, we calculated S in two steps. First, the five hotplate  
275 measurements (electrical power supplied to the plate, ambient temperature, wind speed,  
276 downwelling shortwave flux, and downwelling longwave flux) were input to Eq. 3 in Z18. The  
277 output of that equation is a provisional liquid-equivalent precipitation rate. Second, the snow



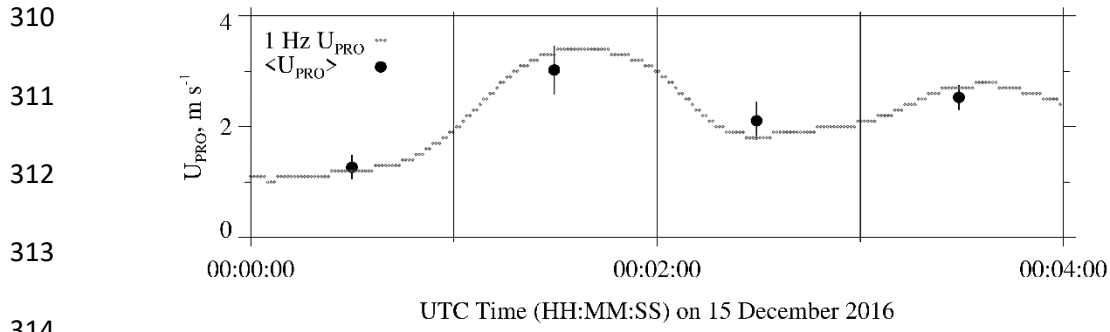
278 particle catch efficiency, described in the next paragraph, was used to calculate  $S$  as the ratio of  
279 the provisional rate and the catch efficiency.

280 Marlow et al. (2023; their Fig. 3b) report the relationship between snow particle catch  
281 efficiency and wind speed that was applied in the calculation of  $S$ . There are three bases for this  
282 relationship. First is the catch efficiencies  $R11$  derived using measurements obtained from a  
283 weighing gauge, operated within a double fence intercomparison reference shield, and collocated  
284 measurements from an unshielded hotplate gauge. These paired measurements are symbolized  
285  $SRG$  (shielded reference gauge) and  $UHG$  (unshielded hotplate gauge).  $R11$  plotted hotplate  
286 catch efficiencies (i.e.,  $UHG/SRG$ ) versus wind speeds measured at 10 m AGL (their Fig. 8).  
287 Second is Marlow et al.'s adjustment of  $R11$ 's 10 m AGL wind speeds to 2 m AGL. The basis  
288 for the adjustment is surface boundary layer parameters derived for  $R11$ 's site (Kochendorfer et  
289 al. 2018) and an equation from Panofsky and Dutton (1984; their Eq. 6.7). The adjustment was  
290 made because the hotplate-derived wind speeds, both here and in Marlow et al. (2023), were  
291 acquired at approximately 2 m above the snowpack surface. Third is Marlow et al.'s comparison  
292 of SNOTEL-derived liquid-equivalent depth changes and hotplate-derived time-integrated  
293 accumulations. The interval for the comparisons is 24 hours. Based on the comparison, which  
294 has 57 paired values acquired at the sites labeled HP and SN in Fig. 1, the average fractional  
295 absolute relative difference is 0.30. Marlow et al. also provided an estimate of the error in a  
296 SNOTEL measurement (2.4 mm). At accumulation = 10 mm the error corresponds to a relative  
297 error = 0.24. This indicates that SNOTEL contributed significantly to the SNOTEL/hotplate  
298 variance and especially so for the smaller accumulations in Fig. 9a of Marlow et al. (2023).  
299 Because of this, we do not limit the following estimate of hotplate precision to a subset of the 57

300 paired measurements. Based on our assessment of the average fractional absolute relative  
301 difference, the hotplate precision applied in this analysis was taken to be 0.3.

302         The hotplate-derived wind speeds acquired at  $\sim 2$  m, and discussed in the previous  
303 paragraph, are henceforth symbolized  $U_{\text{PRO}}$ . The basis for these is a steady state energy budget of  
304 the hotplate's temperature-controlled down-viewing plate and a proprietary algorithm (R11 and  
305 Z18). The  $U_{\text{PRO}}$  are reported by a hotplate as one-minute running averages (Z18) and we  
306 recorded these at 1 Hz. Examples are the gray dots in Fig. 2. Additionally, we calculated and  
307 analyzed one-minute-averaged values of  $U_{\text{PRO}}$  and the corresponding standard deviations.  
308 Examples of these are the black circles and the short vertical line segments in Fig. 2.

309



316 Figure 2 – Hotplate wind speed measurements ( $U_{PRO}$ ) 00:00:00 to 00:04:00 on 15 December

317 2016. Gray dots are the one-minute running-average  $U_{PRO}$  recorded at 1 Hz. Black circles are the

318 one-minute-averaged  $U_{PRO}$  ( $\pm 1$  standard deviation).

### 320 3 - Analysis

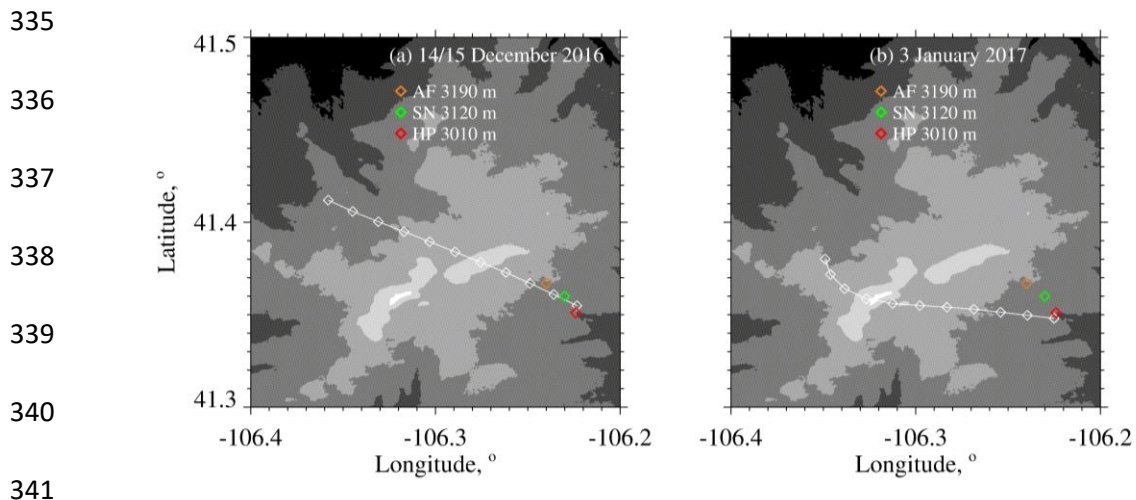
#### 321 3.1 - WKA Overflight Time

322 The focus of our analysis is the two WKA flight segments shown in Figs. 3a-b. The maps  
323 shown in the figures have the three ground sites (AF, SN, and HP) and the WKA flight tracks  
324 (white line). The beginning-to-end time interval for the flight tracks is 100 s and these are  
325 divided into ten 10-second intervals. The 10 s intervals are indicated with white diamonds.  
326 Except for the turn evident in Fig. 3b, the flight tracks are straight, and the track direction is  
327 approximately upwind to downwind.

328 Times that the WKA was closest to the HP site were evaluated by finding the point on the  
329 flight track where the horizontal position of the WKA was closest to the hotplate's coordinates.

330 These times are symbolized  $t_o$  and are referred to as overflight times. In Figs. 3a-b the  
331 downwind end of the flight tracks end at the overflight time. The latitude/longitude position of  
332 the aircraft was within 390 m of the hotplate at the overflight times. Table 1 has the overflight  
333 times on the two flight days.

334



342 Figure 3 – (a) WKA flight track on 14/15 December 2016 for time interval = overflight time -  
 343 100 s to the overflight time. (b) WKA flight track on 3 January 2017 for time interval =  
 344 overflight time - 100 s to the overflight time. The white diamonds on the tracks are separated, in  
 345 time, by 10 s. Altitude thresholds for the digital elevation maps are 2600, 2800, 3000, 3200,  
 346 3400, and 3600 meters. Altitudes of the ground sites are in the legend.

347

### 348 3.2 – Effect of Attenuation on WCR Reflectivities

349

350 ~~(NOTE: Table 3 is at the end of the manuscript)~~

351

352 ~~The presence of water vapor, cloud water, and snow particles within the WCR's transmission~~

353 ~~path will contribute to an attenuation of microwave intensity and will therefore negatively bias~~

354 ~~the retrieved reflectivities (Matrosov 2007; Hiley et al. 2011; Kneifel et al. 2015). We used *in*~~

355 ~~*situ* measurements, and models of attenuation, to estimate this bias. For vapor, we used~~

356 ~~temperature (T), relative humidity (RH), and pressure (P) measurements from the AF (Table 2)~~

357 ~~and an equation for the extinction coefficient (Ulaby et al. 1981; their Eq. 5.22). For cloud water,~~

358 ~~we used T and LWC measurements from the WKA and a parameterized extinction coefficient~~

359 ~~(Liebe et al. 1989; Vali and Haimov 2001). For snow particles, we used 2DP derived snow~~

360 ~~particle mass concentrations, from the WKA, and extinction measurements from Nemerich et. al~~

361 ~~(1988). The snow mass concentrations were evaluated as the product of the 2DP derived snow~~

362 ~~particle volume—assuming spheres—and a snow particle density  $\rho = 210 \text{ kg m}^{-3}$ . This estimate of~~

363 ~~density comes from PV11's  $\rho_+$  formula evaluated at  $D = 1 \text{ mm}$ . Vapor, cloud water, and ice~~

364 ~~particle concentrations applied in the calculations are in the second to fourth columns of Table 3.~~

365 ~~These are the maxima of measurements acquired between  $t_0 - 10 \text{ s}$  and  $t_0$ . This time interval is~~

366 ~~nearly the same as the combined durations of the two WCR averaging intervals analyzed in Sect.~~

367 ~~3.5. The fifth to seventh columns have the one-way transmission pathlengths. For cloud water,~~

368 ~~this is the vertical distance between cloud base [derived thermodynamically using AF~~

369 ~~measurements (Table 2)] and the flight level, and for both vapor and snow particles this is the~~

370 ~~vertical distance between the hotplate and the flight level. (Aircraft and HP altitudes are in Table~~

2 and Fig. 3.) It was assumed that the measured mass concentrations (vapor, cloud water, and snow particles) were uniform over the prescribed pathlengths. Finally, our use of vapor density from the AF ground site is estimated to have caused the vapor-induced attenuations to be overestimated by approximately 50 %. Two-way attenuations ( $\Delta(\text{dB})$ ), summed over contributions from the three components, are presented in the final column. Fortuitously, these are equal on the two days but with vapor and snow particles dominating on December 15 and with liquid water dominating on January 3. Attenuation-corrected reflectivities ( $Z'$ ) were derived using the uncorrected reflectivities ( $Z$ ) and the  $\Delta(\text{dB})$

$$Z' = 10^{\frac{[(10 \cdot \log_{10}(Z) + \Delta(\text{dB})) / 10]}{2}} \quad (1)$$

The presence of molecular oxygen, water vapor, cloud water, and snow particles within the WCR's transmission path will contribute to an attenuation of microwave intensity and will therefore negatively bias the retrieved reflectivities (Matrosov 2007; Hiley et al. 2011; Kneifel et al. 2015). Models of attenuation, radar remote sensing, and in situ measurements were used to calculate this bias. For oxygen, an attenuation coefficient from Ulaby et al. (1981; their Fig. 5.6), and temperature (T) and pressure (P) measurements from the AF (Table 2), were used. For vapor, an attenuation coefficient (Ulaby et al. 1981; their Eq. 5.22), and T, P, and relative humidity (RH) measurements from the AF (Table 2), were used. Concentrations of oxygen and water vapor and the oxygen and vapor path lengths are provided in Table 3. The latter is the vertical distance between the HP and the WKA. It was assumed that concentrations were uniform over this path length.

Attenuation by cloud water was derived using the WKA-measured T (Table 2), the WKA-measured LWC, path length (Table 3), and an attenuation formula (Liebe et al. 1989; Vali

393 and Haimov 2001). The LWC applied in the formula is the maximum of CDP measurements  
394 acquired between  $t_0 - 10$  s and  $t_0$ . This interval coincides with the interval the WCR's down-  
395 looking antenna was used to acquire reflectivities over the HP (Sect. 3.5). The path length for  
396 cloud water was derived as the vertical distance between cloud base [derived thermodynamically  
397 using AF measurements (Table 2)] and flight level. LWC was assumed uniform, at the maximum  
398 value, over the path length.

399 Snow particle mass concentration is typically reported as an ice water content (IWC,  $\text{g m}^{-3}$ )  
400 (Liu and Illingworth 2000). The contribution of IWC to attenuation was calculated using  
401 measurements in Namarich et. al (1988), who reported an attenuation coefficient equal to 0.9  
402 dB/km per unit of IWC. Also used were retrievals of IWC acquired using the down-pointing  
403 WCR antenna. There are several steps in the calculation. First, all profiles of dBZ acquired  
404 between  $t_0 - 10$  s and  $t_0$  were selected. Second, a maximum dBZ was selected at each of the  
405 down-beam range gates (Table 1). Third, the dBZ maxima were increased by the overall two-  
406 way attenuation in the final column of Table 3. Fourth, the profile of attenuation-corrected dBZ  
407 was converted to a profile of attenuation-corrected Z. Fifth, a Z-to-IWC parameterization was  
408 applied ( $\text{IWC} = 0.10 \cdot Z^{0.51}$ ; PV11; their Table 3). Sixth, the IWC profile was integrated, and the  
409 derived ice water path was divided by the snow particle path length (Table 3). This calculation  
410 produced a time- and range-averaged maximum IWC (Table 3). This IWC is the value applied in  
411 the attenuation calculation.

412 Two-way attenuations ( $\Delta dB$ ), summed over contributions from the four components, are  
413 presented in the final column of Table 3. Attenuation by snow and attenuation by liquid were the  
414 most important components ( $> 50$  %) on December 15 and January 3, respectively. Vapor



415 contributed 32 % to the overall on December 15, and the combination of vapor and snow  
416 contributed 45 % on January 3. Equation 1 shows how an attenuation-corrected reflectivity ( $Z'$ )  
417 was derived using an uncorrected reflectivity ( $Z$ ) and the  $\Delta dB$ .

418

419

$$Z' = 10^{\left[\frac{10 \cdot \log_{10}(Z) + \Delta dB}{10}\right]} \quad (1)$$

420 Table 2 – Atmospheric state averages

421

Date	WKA <sup>a</sup> Track Altitude, m	WKA <sup>a</sup> T, °C	AF <sup>b</sup> T, °C	AF <sup>b</sup> RH, %	WKA <sup>a, c</sup> Track Vector	WKA <sup>a, c</sup> Wind Vector	AF <sup>b, c</sup> Wind Vector
14/15 December 2016	4546	-13.9	-6.3	86	310 / 130	274 / 32	250 / 8.5
3 January 2017	4196	-21.7	-14.6	77	280 / 120	265 / 27	260 / 5.4

422

423

424 <sup>a</sup> Altitude, temperature, track vector, and horizontal wind vector data obtained by averaging 1 Hz  
 425 WKA measurements. The averaging interval is 60 s and the interval starts at the overflight time,  
 426 minus 60 s, and ends at the overflight time.

427

428 <sup>b</sup> Temperature (T), relative humidity (RH), and horizontal wind vector data from sensors on the  
 429 US-GLE AmeriFlux tower (Sect. 2.1). The wind sensor was deployed at 26 m AGL (3223 m  
 430 MSL) and the T/RH sensor was deployed at 23 m AGL (3220 m MSL). The AF measurements  
 431 correspond to 30-minute averages closest to the overpass time. In the AF data set time stamps on  
 432 the relevant AF recordings are 00:00 UTC (15 December 2016) and 20:30 UTC (3 January  
 433 2017).

434

435 <sup>c</sup> Vectors are presented in the following format: Direction of motion (degree relative to true  
 436 north) / speed (m s<sup>-1</sup>).

437 Table 3 – Attenuating component concentration, one-way pathlength, and the overall two-way attenuation

Date	Conc. Oxygen, kg m <sup>-3</sup>	Conc. Vapor, kg m <sup>-3</sup>	Maximum LWC, g m <sup>-3</sup>	Maximum IWC, g m <sup>-3</sup>	One-way Pathlength <sup>a</sup> Oxygen, Vapor, and Snow, km	One-way Pathlength <sup>b</sup> Cloud Water, km	Overall Two-way Attenuation, ΔdB
15 December 2016	0.21	2.7x10 <sup>-3</sup>	0.01	0.27	1.54	1.09	1.41 <sup>c</sup>
3 January 2017	0.21	1.3x10 <sup>-3</sup>	0.08	0.09	1.19	0.59	1.01 <sup>d</sup>

438

439 <sup>a</sup> Vertical distance between HP and WKA

440

441 <sup>b</sup> Vertical distance between cloud base [derived thermodynamically using AF measurements (Table 2)] and WKA

442

443 <sup>c</sup> One-way attenuation coefficients are 0.03 dB/km for oxygen (Ulaby et al. 1981), 0.14 dB/km for vapor (Ulaby et al. 1981), 0.056  
444 dB/km for cloud water (Liebe et al. 1989; Vali and Haimov 2001), and 0.24 dB/km for snow particles (Nemarich et. al 1988).

445

446 <sup>d</sup> One-way attenuation coefficients are 0.03 dB/km for oxygen (Ulaby et al. 1981), 0.073 dB/km for vapor (Ulaby et al. 1981), 0.49  
447 dB/km for cloud water (Liebe et al. 1989; Vali and Haimov 2001), and 0.077 dB/km for snow particles (Nemarich et. al 1988).

448



### 450 3.3 - Correction of Doppler Velocity

451 We accounted for bias in  $V_D$  (Sect. 2.3) due to deviation of the down-looking WCR  
 452 antenna from vertical. This was done by applying the correction described in Zaremba et al.  
 453 (2022) (their Eq. A4). The west-to-east and south-to-north particle velocities used in the  
 454 correction were assumed to be equal to component wind velocities. The latter were expressed as  
 455 linear functions of altitude using the information in the penultimate and last columns of Table 2.  
 456 The component velocities as functions of altitude and the linear equations relating velocity and  
 457 altitude are provided in the Appendix.

### 458 3.4 - Hotplate Measurement of Wind Speed

459 Here we compare the hotplate-derived wind speed to wind speed derived using an  
 460 R.M.Young rotating anemometer (R.M.Young 2001). The second of these is symbolized  $U_{RMY}$   
 461 and the basis for the first ( $U_{PRO}$ ) is a proprietary algorithm (Sect. 2.4). We are doing this  
 462 comparison because B14 showed that  $U_{PRO}$  can be high-biased, relative to a conventional  
 463 anemometer, and because  $U_{PRO}$  is the primary determinant of the rate that the up-viewing plate  
 464 dissipates sensible heat energy. Diagnosis of that heat transfer rate is our basis for calculating the  
 465 liquid-equivalent snowfall rate (Z18). The  $U_{PRO}$  also determines the snow particle catch  
 466 efficiency and the latter was used in calculations of the undercatch-corrected liquid-equivalent  
 467 snowfall rate (Sect. 2.4).

468 ~~Three years before the wind speed comparison presented here, we attempted to compare~~  
 469 ~~the  $U_{PRO}$  reported by our hotplate<sup>3</sup> and wind speed reported by a WXT520 Vaisala weather~~  
 470 ~~transmitter equipped with an ultrasonic anemometer (Vaisala 2012). These instruments were~~

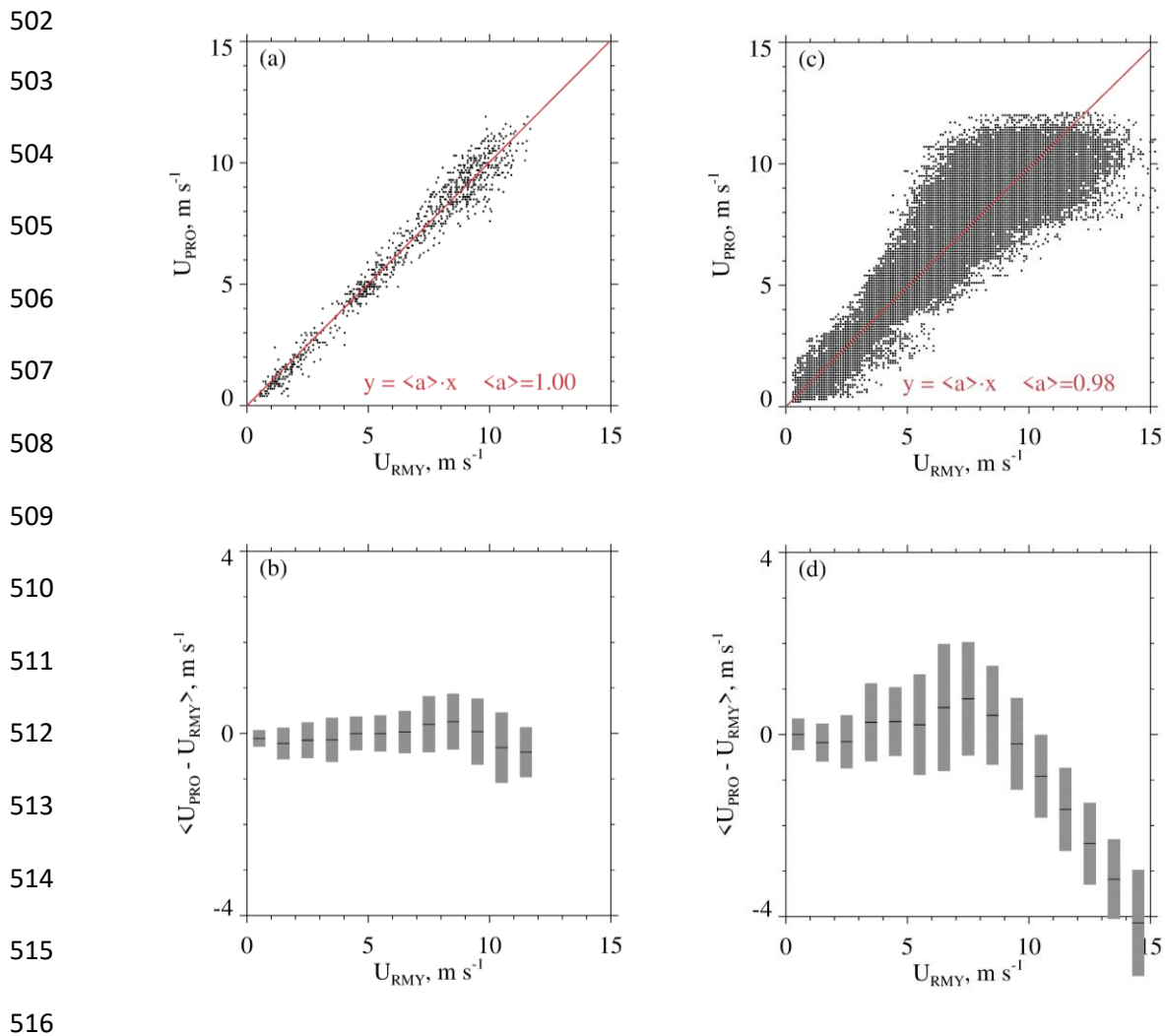
---

<sup>3</sup>~~The hotplate used here is the device described in Wolfe and Snider (2012), in Z18, and in Marlow et al. (2023).~~

471 ~~operated at the HP site in Fig. 1b. However, that data set was difficult to interpret because we did~~  
472 ~~not correctly record the desired 1 Hz wind speed measurements from the WXT520.~~ The  
473 comparisons reported here ~~were~~ was done at the Laramie, WY Airport in December 2019, and in  
474 January 2020. Compared to the HP site, the Laramie Airport site (indicated LA in Fig. 1) is free  
475 of obstruction, out to 120 m, and experiences larger wind speeds. By mounting the hotplate and  
476 the R.M.Young anemometer on rigid metal pipes, the hotplate's heated horizontal surfaces (the  
477 up- and down-viewing plates seen in Fig. ~~ure~~ 1 of Z18) and the anemometer's spinning axis  
478 (oriented horizontally) were both positioned at 2 m AGL. The pipes were separated horizontally  
479 by 5 m. There was no precipitation on the days selected for the wind speed comparisons. The  
480 values of  $U_{\text{PRO}}$  and  $U_{\text{RMV}}$  we analyzed were recorded with a data system that time stamped the 1  
481 Hz  $U_{\text{PRO}}$  and 1 Hz  $U_{\text{RMV}}$  with a relative timing accuracy no worse than 1 s.

482 A wind speed comparison - from 13 December 2019 - is shown in Fig. 4a.  $U_{\text{PRO}}$  was  
483 brought into the comparison by sampling it once per minute from files containing 1 Hz  
484 recordings of the one-minute running-average  $U_{\text{PRO}}$  (Sect. 2.4).  $U_{\text{RMV}}$  was brought into the  
485 comparison by starting with files containing 1 Hz recordings and converting these to one-minute  
486 averages. Fig. 4a shows no evidence of bias and Fig. 4b demonstrates that the average absolute  
487 departure between the  $U_{\text{PRO}}$  and  $U_{\text{RMV}}$  (both one-minute averages) is no larger than  $0.5 \text{ m s}^{-1}$ .  
488 Table 4 has eight more precipitation-free comparisons. Included in the table are temperature and  
489 wind speed averaged over the comparison intervals (4 to 20 UTC), the slope of the linear-least-  
490 squares fit line (forced through the origin, red line), and the lower and upper quartiles of the  
491 slope. The quartiles were calculated using the method of Wolfe and Snider (2012). In contrast to  
492 Figs. 4a-b, Figs. 4c-d make the comparison using 1 Hz values of  $U_{\text{PRO}}$  and  $U_{\text{RMV}}$ . The larger  
493 scatter and larger average absolute departure seen in these panels is a consequence of the

494 hotplate's limited time response, compared to the R.M.Young. We quantify the hotplate's  
495 response time in terms of a calculated thermal response time. During wintertime at the Laramie  
496 Airport, and with wind speed at  $5 \text{ m s}^{-1}$ , the down-viewing plate's thermal response time is  
497 approximately 60 s (results not shown). Because the temperature of the down-viewing plate is  
498 actively controlled, this does not translate to a 60 s lag between changes in wind speed and the  
499 hotplate response. The  $U_{\text{PRO}}/U_{\text{RMY}}$  departure is most evident at  $U_{\text{PRO}} > 5 \text{ m s}^{-1}$  (Fig. 4d) but this is  
500 not a concern for  $U_{\text{PRO}}$  on 14/15 December 2016 or on 3 January 2017. Snider (2023)  
501 demonstrated that the  $U_{\text{PRO}}$  was less than  $5 \text{ m s}^{-1}$  at the hotplate during the two WKA overflights.



517 Figure 4 – (a) Scatterplot of one-minute-averaged  $U_{\text{PRO}}$  and one-minute-averaged  $U_{\text{RMY}}$ .  
 518 Measurements were acquired at the Laramie, WY Airport 13 December 2019. The red line is a  
 519 linear-least-squares fit line (forced through the origin). (b) Average departure between one-  
 520 minute-averaged  $U_{\text{PRO}}$  and one-minute-averaged  $U_{\text{RMY}}$ . Average departures were calculated for  
 521 discrete  $U_{\text{RMY}}$  intervals, and the averages are indicated with short black horizontal lines. Gray  
 522 bars indicate  $\pm 1$  standard deviation. (c) Same as in (a) except 1 Hz values of  $U_{\text{PRO}}$  and  $U_{\text{RMY}}$ . (d)  
 523 Same as in (b) except for 1 Hz values of  $U_{\text{PRO}}$  and  $U_{\text{RMY}}$ .

524



525

526 Table 4 -  $U_{\text{PRO}}$  versus  $U_{\text{RMY}}$  correlations

527

Date, UTC <sup>1</sup>	$\langle T \rangle^2$ , °C	$\langle U \rangle^2$ , m s <sup>-1</sup>	$\langle a \rangle^3$	a <sup>4</sup> First Quartile	a <sup>4</sup> Third Quartile
7 December 2019	-0.40	5.40	1.00	0.90	1.04
8 December 2019	2.70	4.10	0.99	0.90	1.04
10 December 2019	-5.20	3.80	0.99	0.83	1.04
13 December 2019	-1.50	6.60	1.00	0.93	1.06
18 December 2019	-6.20	3.60	0.99	0.92	1.04
19 December 2019	-6.90	2.70	0.95	0.84	0.99
6 January 2020	-6.40	8.80	1.01	0.96	1.06
8 January 2020	0.30	4.20	1.00	0.87	1.05
11 January 2020	-7.20	7.00	1.02	0.97	1.08

528

529

530 <sup>1</sup> Statistics presented are based on one-minute-averaged  $U_{\text{PRO}}$  and one-minute-averaged  $U_{\text{RMY}}$ 

531 measurements made between 04:00 to 20:00 UTC.

532

533 <sup>2</sup> Interval-averaged temperature and interval-averaged wind speed.

534

535 <sup>3</sup> Slope of the one-minute-averaged  $U_{\text{PRO}}$  versus one-minute-averaged  $U_{\text{RMY}}$  linear-least-squares

536 fit line, forced through the origin.

537

538 <sup>4</sup> Quartiles of the slope (see text)

539

### 540 3.5 – Combined Aircraft and Surface Measurements

541 Figure 5 has WCR and WKA measurements starting 100 s prior to  $t_o$  and ending at  $t_o$ .  
542 The sequences in Figs. 5a and 5c are reflectivities from both the up- and down-looking antennas.  
543 In Fig. 5a the flight track (black dashed horizontal line) is at 4550 m and in Fig. 5c the flight  
544 track is at 4200 m. At the  $t_o$  in Fig. 5a, below the WKA, the maximum radar echo is +6 dBZ ( $Z =$   
545  $4 \text{ mm}^6 \text{ m}^{-3}$ ) and in Fig. 5c the maximum is -3 dBZ ( $Z = 0.5 \text{ mm}^6 \text{ m}^{-3}$ ). Supercooled liquid water  
546 was detected as the aircraft approached the ridgeline (Fig. 5b) and during the last 10 seconds of  
547 the time sequence in Fig. 5d. During these encounters with supercooled liquid, the maximum  
548 LWC values were  $0.03 \times 10^{-3}$  and  $0.08 \times 10^{-3} \text{ kg m}^{-3}$  on 14 December 2016 and 3 January 2017,  
549 respectively. Values of  $N$  (Sect. 2.2) at times of maximal LWC were  $3 \times 10^6$  and  $100 \times 10^6 \text{ m}^{-3}$  on  
550 14 December 2016 and 3 January 2017, respectively. Even on 3 January 2017, the  $\langle D \rangle$  (Sect.  
551 2.2) associated with maximum LWC was sufficient for hexagonal plate crystals with diameter  
552 larger than  $100 \text{ }\mu\text{m}$  to collide with the observed droplets with efficiencies  $> 0.1$  (Wang and Ji  
553 2000).

554 We temporally and spatially averaged the values of  $Z$  we compared with time-averaged  
555 values of  $S$ . There are two reasons for this: 1) As discussed in Sect. 3.1, the WCR did not sample  
556  $Z$  exactly over the hotplate, and furthermore, the width of radar beam at 1500 m range - roughly  
557 the distance between the aircraft and the ground at the overflight times - is 30 m and thus  
558 considerably smaller than the minimum horizontal distance between the aircraft and the HP. 2)  
559 Compared to the WCR, the hotplate is a relatively slow-response measurement system whose  
560 output is commonly averaged over one-minute intervals (Z18).

561

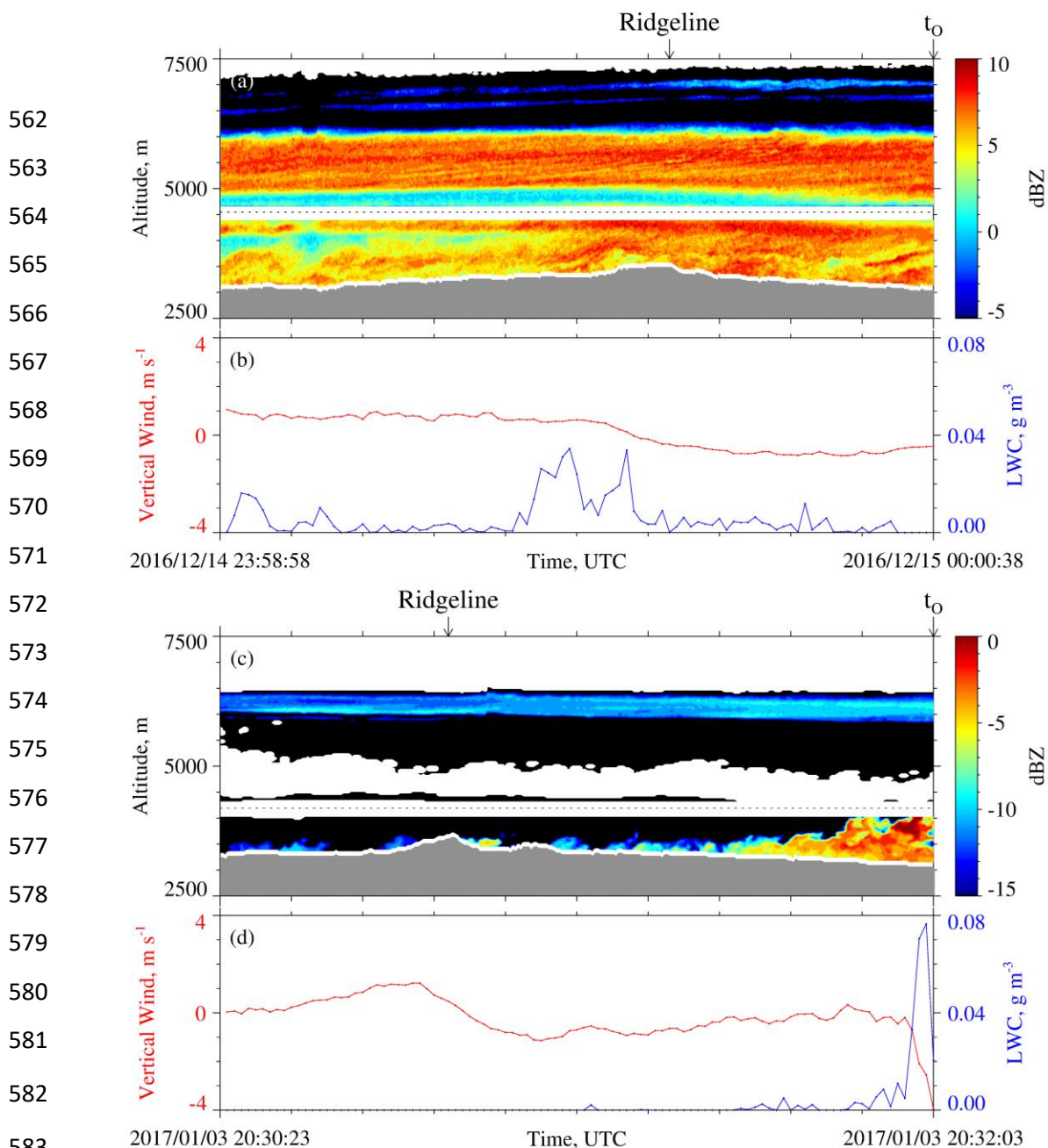


Figure 5 – (a) 100 s of WCR reflectivity and (b) 100 s of LWC and gust probe vertical wind velocity ending at  $t_0$  on 14/15 December 2016. (c) 100 s of WCR reflectivity and (d) 100 s of LWC and gust probe vertical wind velocity ending at  $t_0$  on 3 January 2017. In (a) and (c), above and below the flight track, is the roughly 200-m-deep WCR blind zone, reflectivity above (below) the flight track is from the up-looking (down-looking) WCR antenna, black indicates dBZ values smaller than minimum indicated in the color bar, white immediately above the terrain indicates echo that was discarded because of ground clutter, and white above the ground clutter and outside of the blind zone indicate dBZ < minimum detectable signal.

594           The HP measurements were averaged over two adjacent 60 s intervals. The first extends  
595 from  $t_0$  to  $t_0 + 60$  s (Fig. 6a) and the second from  $t_0 + 60$  s to  $t_0 + 120$  s (Fig. 6c). In Fig. 6a and  
596 in Fig. 6c,  $t_{HP,B}$  symbolizes an interval's beginning time and  $t_{HP,E}$  symbolizes an interval's  
597 ending time. Formulas describing how these times were related to the beginning and ending time  
598 of a corresponding WCR averaging interval are in the Appendix. Fig. 6b is a schematic of the  
599 first WCR averaging interval and Fig. 6d is a schematic of the second. Again, the subscripts "B"  
600 and "E" are used to indicate averaging beginning and ending times. Figures 6b and 6d both have  
601 lines at the top of an averaging interval/domain. The slopes of these lines are proportional to the  
602 ratio of two speeds. These speeds are a maximum likely snow particle speed toward the ground (  
603  $v_p$ ) and a horizontal wind advection speed ( $v_w$ ). The  $v_p$  was calculated using averaged vertical-  
604 component Doppler velocities and  $v_w$  was calculated using a vertical profile of horizontal winds,  
605 based on WKA horizontal wind measurements and AF horizontal wind measurements (Figs.  
606 A1a-b), and using the WKA track vector (Table 2). An altitude ( $z' = 3400$  m) was assumed in the  
607 calculation of  $v_w$ . This is the altitude of the ridges west and northwest of the HP site (Figs. 3a-  
608 b). Picking the altitude to be either  $z' = 3200$  m or  $z' = 3600$  m does not alter our findings.  
609

610  
 611  
 612  
 613  
 614  
 615  
 616  
 617  
 618  
 619  
 620  
 621  
 622  
 623  
 624  
 625  
 626  
 627  
 628  
 629  
 630  
 631  
 632  
 633  
 634

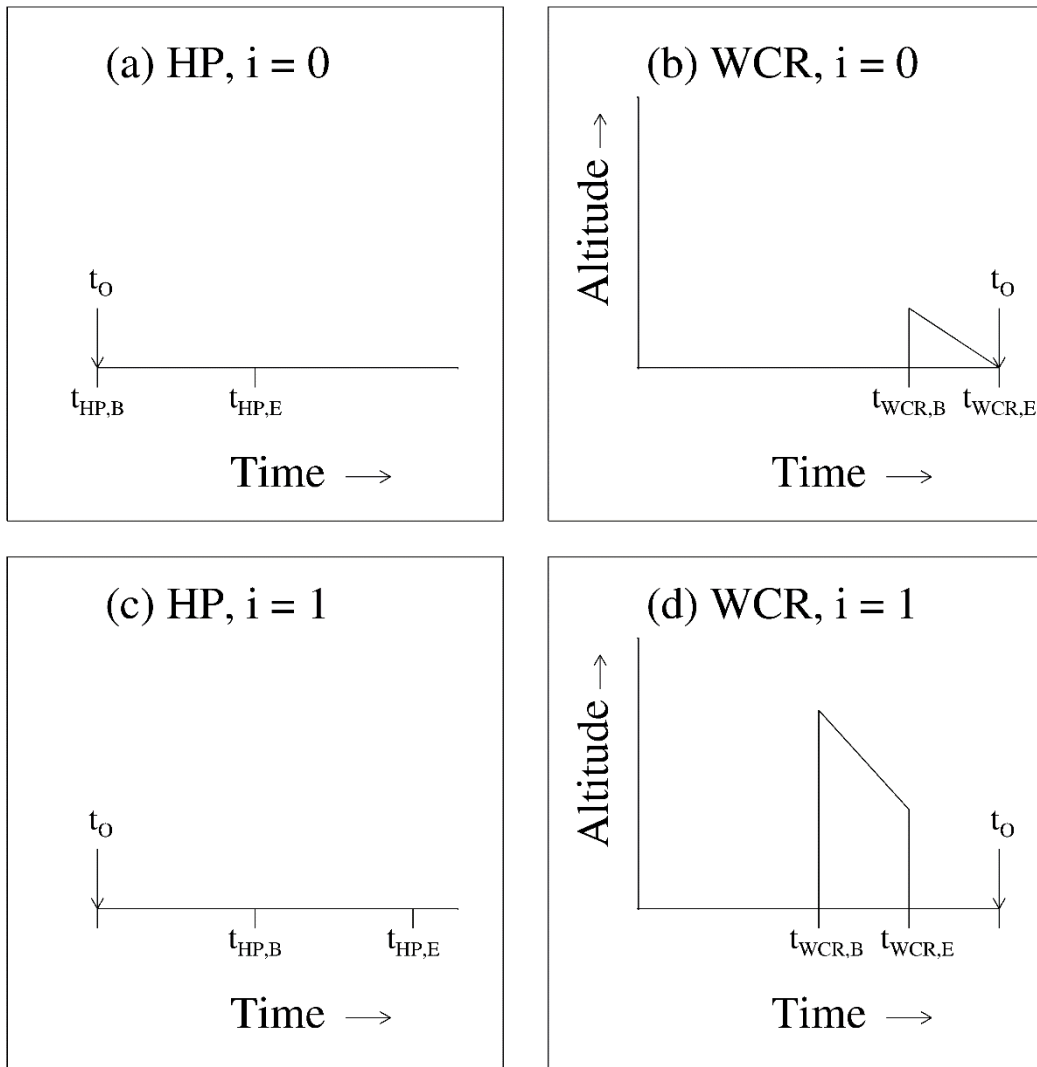


Figure 6 – (a and c) Representations of the  $i = 0$  and  $i = 1$  HP averaging intervals. (b and d) Representations of the  $i = 0$  and  $i = 1$  WCR averaging intervals/domains. The  $t_0$  is shown in all panels. The subscripts “B” and “E” indicate beginning and ending times of HP averaging (panels a and c) and the beginning and ending times of WCR averaging (panels b and d).

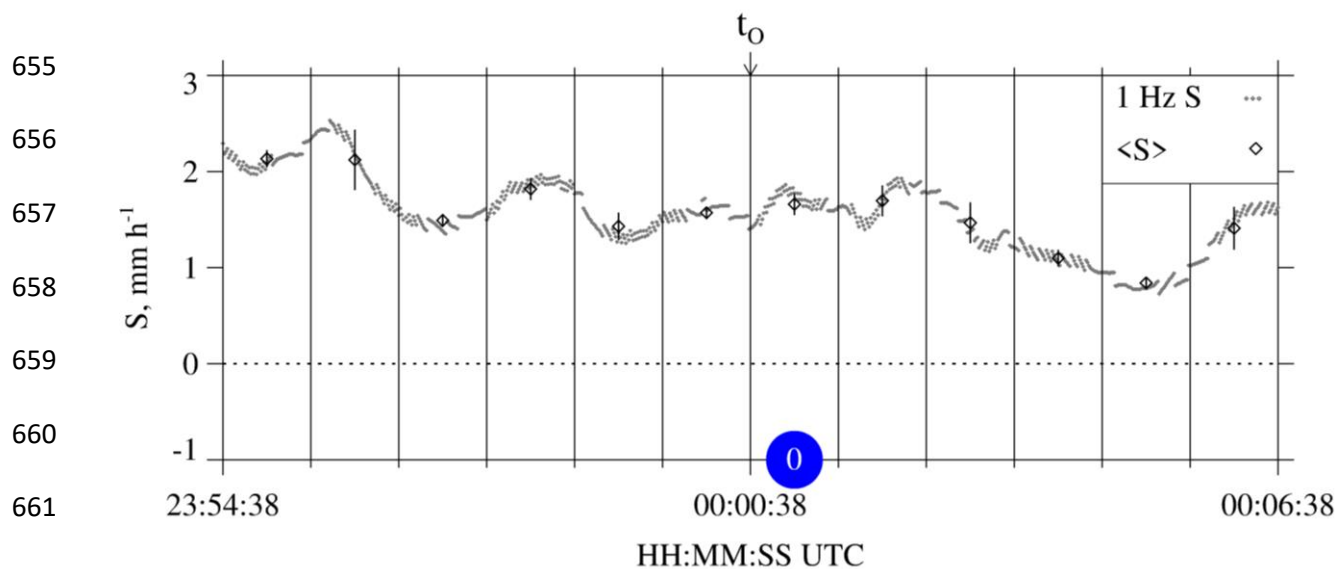
635

636 All panels in Fig. 6 are labeled with an index designating either the first averaging  
637 interval ( $i = 0$ ) or the second averaging interval ( $i = 1$ ). Figures 7 and 8 present  
638 hotplate snowfall measurements from 14/15 December 2016 and 3 January 2017. In these, and in  
639 subsequent figures, colored circles surround the indexes, blue is used to color-code 15 December  
640 2016, and red is used to color-code 3 January 2017. Additionally, Fig. 8 has an  $i = 2$  averaging  
641 interval. This is a special case discussed at the end of this section.

642 Figures 9a-b and Figs. 10a-b have enlarged views of the altitude-time crosssections  
643 recorded on the two flight days. Different from Fig. 5a and Fig. 5c, these measurements are only  
644 from the WCR's down-looking antenna. Additional differences are the following: 1) The plots  
645 are set up so that Z and  $V_D$  structures downwind of the hotplate can be seen. These structures are  
646 discussed in the following section. 2) The WCR measurements are shown for 50 s of flight. With  
647 the WKA ground speed approximately  $125 \text{ m s}^{-1}$  (Table 2), the distance along the abscissa is  
648 6250 m. 3) Colored circles that surround the  $i = 0$  index are placed below the WCR averaging  
649 intervals/domains. The latter are drawn with solid black lines and are seen to overlay both the Z  
650 and  $V_D$  altitude-time crosssections. Consistent with Figs. 6b and 6d, and the Appendix, one of  
651 these black lines is vertical and the other is negatively sloped. Figs. 10a-b also have the  $i = 2$   
652 intervals/domains discussed at the end of this section.

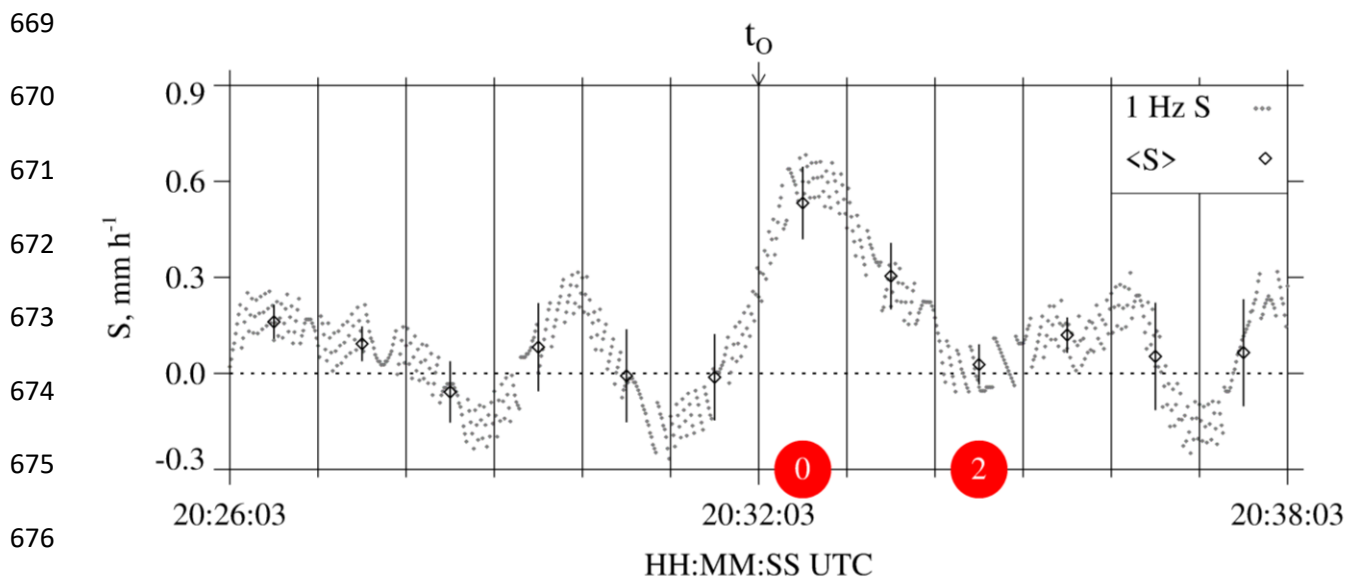
653

654



664 Figure 7 – Twelve minutes of HP snowfall measurements from 14/15 December 2016. Gray dots  
 665 are  $S$  values calculated using hotplate output recorded at 1 Hz. Black diamonds are the one-  
 666 minute-averaged values ( $\pm 1$  standard deviation). The  $t_0$  is shown above the panel and the blue  
 667 circle designates the  $i = 0$  HP averaging interval.

668



679 Figure 8 – Twelve minutes of HP snowfall measurements from 3 January 2017. Gray dots are  $S$

680 values calculated using hotplate output recorded at 1 Hz. Black diamonds are the one-minute-

681 averaged values ( $\pm 1$  standard deviation). The  $t_0$  is shown above the panel, a red circle designates

682 the  $i = 0$  HP averaging interval, and a red circle designates the  $i = 2$  HP averaging interval. The

683 latter is a special case discussed at the end of Sect. 3.5.



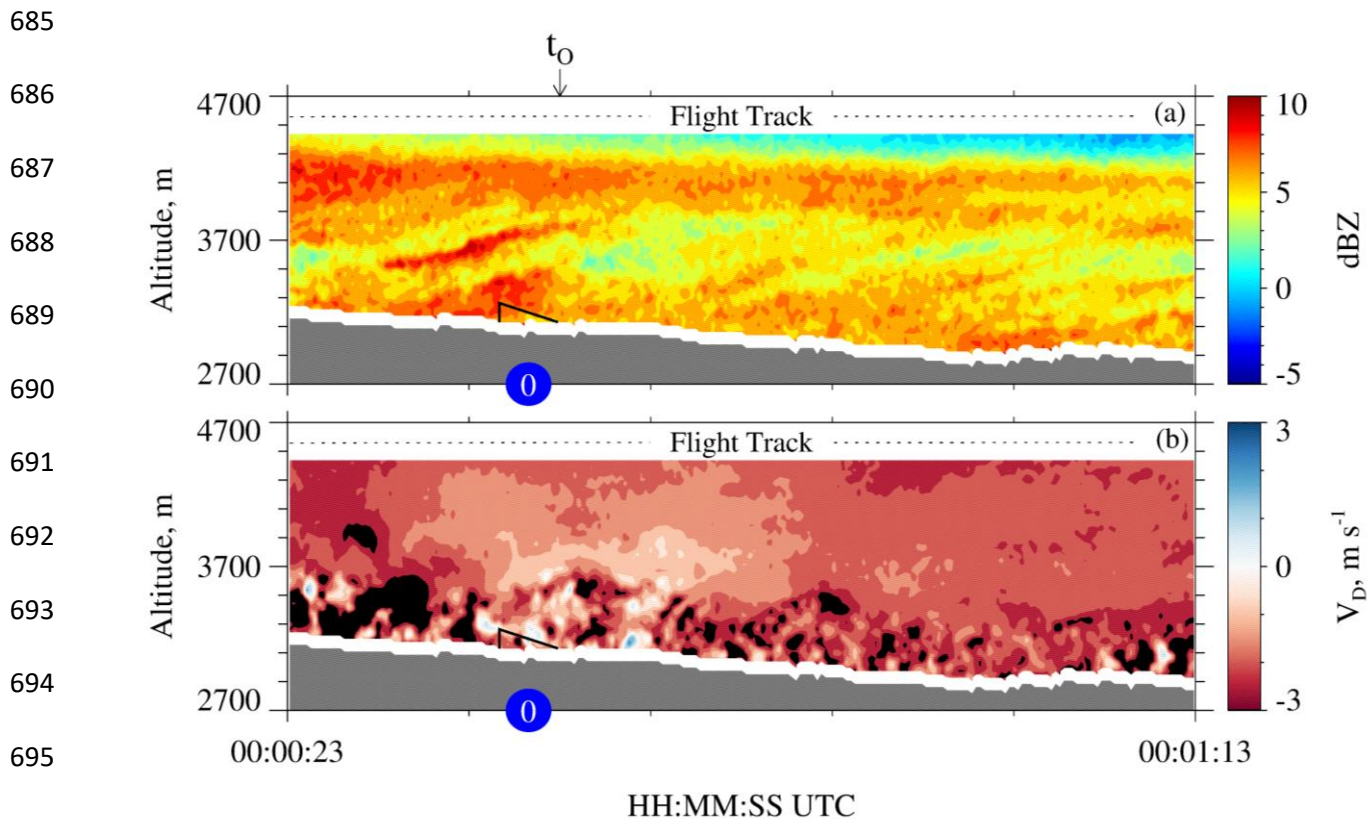


Figure 9 – 50 s of measurements from the down-looking WCR antenna on 15 December 2016.

(a) Cross-section of reflectivity  $t_0 - 15$  s to  $t_0 + 35$  s. (b) Cross-section of Doppler velocity  $t_0 - 15$  s to

$t_0 + 35$  s. The  $t_0$  is shown above the top panel. In both panels, the solid black lines (vertical and

sloped) encompass the  $i = 0$  WCR averaging interval/domain and blue circles designate the

$i = 0$  WCR averaging interval.

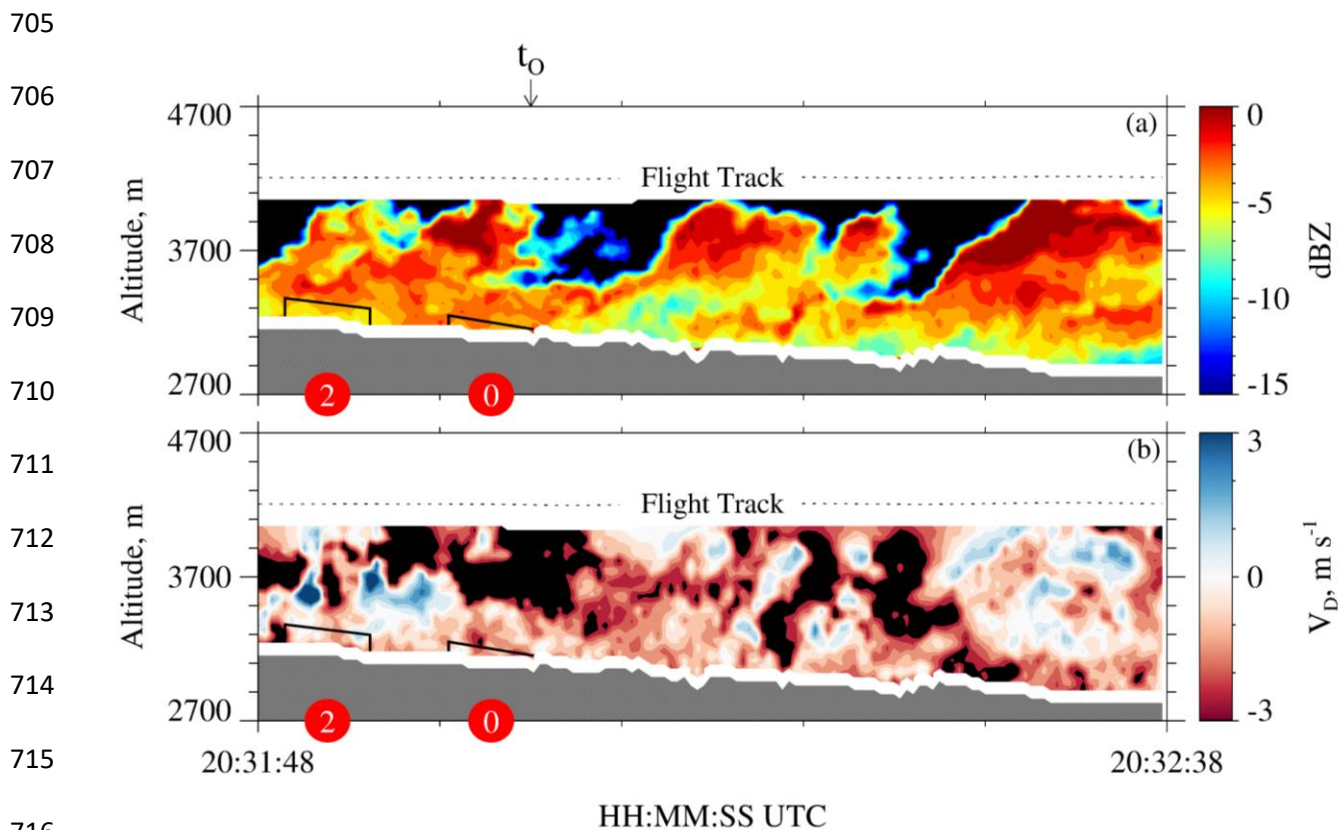


Figure 10 – 50 s of measurements from the down-looking WCR antenna on 3 January 2017. (a) Crossection of reflectivity  $t_0 - 15$  s to  $t_0 + 35$  s. (b) Crossection of Doppler velocity  $t_0 - 15$  s to  $t_0 + 35$  s. The  $t_0$  is shown above the top panel. In both panels, the solid black lines (vertical and sloped) encompass the  $i = 0$  and  $i = 2$  WCR averaging intervals/domains, two red circles designate the  $i = 0$  WCR averaging interval, and two red circles designate the  $i = 2$  WCR averaging interval. The  $i = 2$  intervals/domains are a special case discussed at the end of Sect. 3.5.

726 The  $i = 0$   ~~$i = 0$~~  averages of S and Z are presented in Table 5 and the corresponding  
 727 averaging intervals are viewable in Fig. 7 and Fig. 9a (15 December 2016) and in Fig. 8 and Fig.  
 728 10a (3 January 2017). The  $i = 1$   ~~$i = 1$~~  averages are also presented in Table 5. According to the  
 729 averaging scheme (Fig. 6), the  $i = 1$   ~~$i = 1$~~  HP averaging interval is time-shifted positively  
 730 compared to the  $i = 0$   ~~$i = 0$~~  HP averaging interval and the  $i = 1$   ~~$i = 1$~~  WCR averaging interval is  
 731 time-shifted negatively compared of the  $i = 0$   ~~$i = 0$~~  WCR averaging interval. This arrangement  
 732 of the averaging intervals is one way to average while also accounting for wind advection of the  
 733 snow particles.

734 As discussed earlier in this section, the averaging scheme initializes with 60-second  
 735 blocks of HP data between  $t_0$  and  $t_0 + 120$  s. When we applied the scheme to data from 3 January  
 736 2017, but outside the specified time range, an inconsistency was documented. This is apparent in  
 737 Fig. 8, where the  $t_0 + 120$  s to  $t_0 + 180$  s interval (i.e., the  $i = 2$  interval) has negligible average S,  
 738 while in Fig. 10, the  $i = 2$  interval has a non-negligible average Z ( $\sim 0.3 \text{ mm}^6 \text{ m}^{-3}$ ). A firm  
 739 explanation is not available for the inconsistency, but a factor may be the convective nature of  
 740 the fields in Figs. 10a-b. Because of the inconsistency, only averages corresponding to the  $i = 0$   
 741 and  $i = 1$  intervals were analyzed further.

742

743

744 Table 5 – Averaged wind, hotplate, and WCR measurements

Date	$v_w^a$ , m s <sup>-1</sup>	i index	$\langle S \rangle \pm \sigma_S^b$ , mm h <sup>-1</sup>	WCR Samples <sup>c</sup>	$\langle V_D \rangle^d$ , m s <sup>-1</sup>	$\sigma_{V_D}^e$ , m s <sup>-1</sup>	$v_p^f$ , m s <sup>-1</sup>	$\langle Z \rangle \pm \sigma_Z^g$ , mm <sup>6</sup> m <sup>-3</sup>
15 December 2016	7.4	0	1.7±0.1	42	-1.3	0.9	2.2	4.9±2.1
15 December 2016	7.4	1	1.7±0.2	149	-1.8	1.2	3.0	5.6±1.1
3 January 2017	8.9	0	0.5±0.1	22	-0.9	0.8	1.7	0.49±0.05
3 January 2017	8.9	1	0.3±0.1	35	-0.8	0.4	1.2	0.50±0.10

745

746 <sup>a</sup> Horizontal wind advection speed (Eq. A7) calculated using values from the penultimate and last  
747 columns of Table 2.

748

749 <sup>b</sup> One-minute average of the undercatch-corrected liquid-equivalent snowfall rate ( $\pm 1$  standard  
750 deviation). An example averaging interval is the  $i = 0$  interval in Fig. 7.

751

752 <sup>c</sup> Number of samples used to calculate WCR statistics in the penultimate four columns. The  
753 averaging intervals/domains (e.g.,  $i = 0$   ~~$i = 0$~~   ~~$i = 0$~~  in Figs. 9a-b and in Figs. 10a-b) encompass  
754 the averaged WCR samples.

755

756 <sup>d</sup> Average of Doppler velocity within the averaging intervals/domains.

757

758 <sup>e</sup> Standard deviation of Doppler velocity within the averaging intervals/domains.

759

760 <sup>f</sup> Maximum likely snow particle speed toward the ground (Eq. A8).

761

762 <sup>g</sup> Average reflectivity ( $\pm 1$  standard deviation). These values are not corrected for attenuation.

763

### 764 3.6 - Snow Particle Imagery

765 In Fig. 9a and Fig. 10a, the time for a snow particle to move the abscissa and ordinate  
 766 distances is different. The ratio of these two times is 2.6. This follows from our choice of  
 767 abscissa and ordinate ranges, from values of particle fall speed ( $1 \text{ m s}^{-1}$ ) and horizontal wind  
 768 advection speed ( $8 \text{ m s}^{-1}$ ), which we assumed, and from the WKA ground speed ( $g_s \sim 125 \text{ m}$   
 769  $\text{s}^{-1}$ ; Table 2). The assumed values are approximately consistent with values of  $\langle V_D \rangle$  and  $v_w$ , in  
 770 Table 5, and with the  $V_D$  sign convention (Sect. 2.3). We also used  $g_s = 125 \text{ m s}^{-1}$  to scale  
 771 (virtually) the time axes in Fig. 9a and Fig. 10a to a horizontal distance. Within the scaled  
 772 coordinate frames, we assumed that all snow particle trajectories have negative slope ( $\Delta z / \Delta x = -$   
 773  $1 \text{ m s}^{-1} / 8 \text{ m s}^{-1} = -0.12$ ) and that all trajectories are stationary. However, both assumptions seem  
 774 inconsistent with the reflectivity structures in Fig. 5a, where positively-sloped particle fall  
 775 streaks are evident at  $\sim 5500 \text{ m}$ , inconsistent with Fig. 9a where positively-sloped fall streaks are  
 776 at  $\sim 3500 \text{ m}$ , and inconsistent with the positively-sloped fall streaks in Fig. 10a. On both flight  
 777 days, the fall streaks evince particle sources that move horizontally and with a horizontal speed  
 778 that is larger than the  $v_w = 8 \text{ m s}^{-1}$  applied in the estimate of the trajectory slope. It may be that  
 779 the source's horizontal speed is comparable to the flight-level WKA-derived horizontal wind (27  
 780 to  $32 \text{ m s}^{-1}$ ; Table 2) but we do not have data needed to verify that assertion. Based on the  
 781 assumption that snow particles followed the fall streaks while both were advecting horizontally,  
 782 we looked *downwind* of the hotplate - at a time later than  $t_o$  in Fig. 9a and Fig. 10a - for particles  
 783 that became those that produced snowfall at the hotplate.

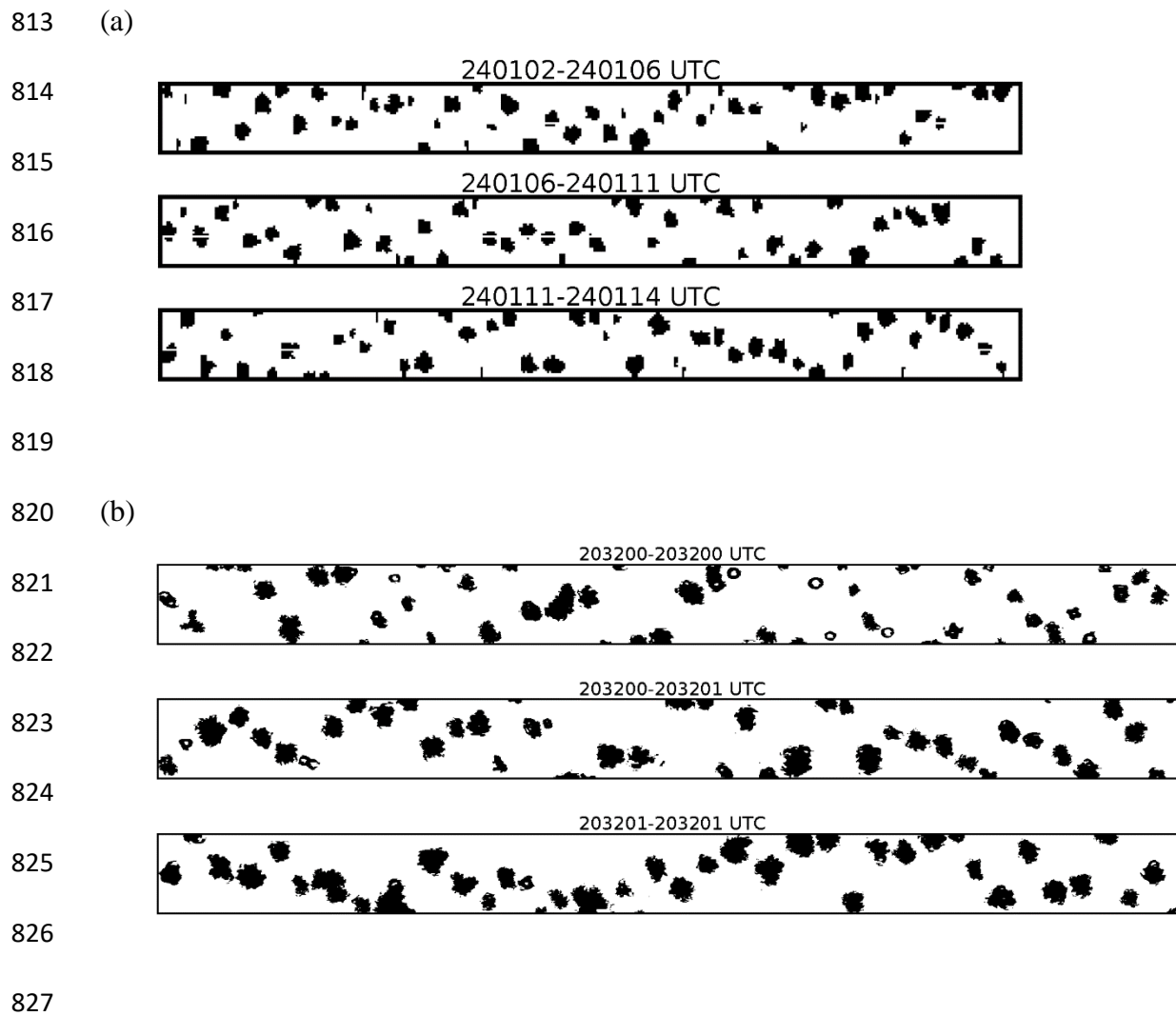
784 Particle images from 15 December 2016 were analyzed using the 2DP. With this  
 785 instrument the maximum all-in particle size (in the horizontal direction perpendicular to flight) is

786 6400  $\mu\text{m}$  and the particle size resolution is 200  $\mu\text{m}$  (Sect. 2.2). Within the time interval picked  
787 for this analysis (discussed below), particles sizing in the smaller of the two spectral modes, with  
788 mode size  $\sim 400 \mu\text{m}$ , were more numerous (results not shown). Because the 400  $\mu\text{m}$  particles are  
789 poorly resolved by the 2DP, and the same can be said for somewhat larger particles, those  
790 smaller than 1000  $\mu\text{m}$  were excluded from the following analysis. Figure 11a shows imagery  
791 from 12 s of measurements acquired near the end of the sequence in Fig. 9a (00:01:02 to  
792 00:01:14). This time interval was selected by tracing forward from  $t_0$ , along the slope of the fall  
793 streaks, to the flight level. Many of the particles are rounded (indicating riming) and a few have  
794 arms likely due to incomplete conversion of branched crystals to rimed snow particles. The mode  
795 size corresponding to these images is 1600  $\mu\text{m}$ . No liquid water was detected with these particles  
796 (LWC  $< 0.01 \times 10^{-3} \text{ kg m}^{-3}$ ; Fuller 2020; her Fig. 8), but liquid was detected, at  $\sim 00:00:00$ , as  
797 the aircraft approached the ridgeline (Figs. 5a-b).

798 Turning to imagery from 3 January 2017, the most appropriate location for analysis  
799 would be through the second billow structure evident in Fig. 10a. This billow sourced a fall  
800 streak that terminated at the hotplate (i.e., at the time  $t_0$  indicated in the figure). However, the  
801 aircraft only clipped the top of this billow, and it was only when sampling the billow seen  $\sim 13$  s  
802 earlier that larger ice particle concentrations ( $\sim 20,000 \text{ m}^{-3}$ ) (Fuller 2020; her Fig. 10) and  
803 larger LWC ( $\sim 0.08 \times 10^{-3} \text{ kg m}^{-3}$ ; Fig. 5d) were detected. Maximum reflectivities were the same  
804 in all three billows ( $Z \sim 1 \text{ mm}^6 \text{ m}^{-3}$ ; 0 dBZ), so it was assumed that imagery collected in the first  
805 billow (20:32:00 to 20:32:02) was representative of what was falling toward the hotplate. The  
806 2DS was used to image these particles (Fig. 11b); with this instrument the maximum all-in  
807 particle size (in the horizontal direction perpendicular to flight) is 1280  $\mu\text{m}$  and the size  
808 resolution is 10  $\mu\text{m}$  (Sect. 2.2). Most of the objects in Fig. 11b appear to be rimed and their mode

809 size is  $\sim 400 \mu\text{m}$ . It is also noted that particles smaller than  $100 \mu\text{m}$  were eliminated from these  
810 images, however, compared to the  $\sim 400 \mu\text{m}$  particles those smaller than  $100 \mu\text{m}$  were  
811 significantly less abundant (results not shown).

812



828 Figure 11 – (a) 2DP particle imagery from 15 December 2016. The height of the strips is 6400  
829  $\mu\text{m}$ . These particles are estimated to be representative of those that fell from flight level toward  
830 the hotplate. (b) 2DS particle imagery from 3 January 2017. The height of the strips is 1280  $\mu\text{m}$ .  
831 These particles are estimated to be representative of those that fell from flight level toward the  
832 hotplate.

833



834 **3.7 – S/Z Relationships**

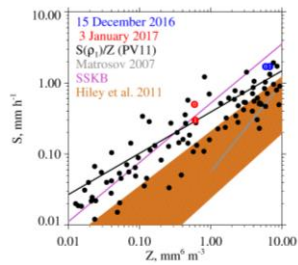
835 ~~Our S/Z pairs are presented in Table 5 where the indexes ( $i=0$  and  $i=1$ ) are used to~~  
836 ~~indicate results derived for the averaging intervals. Here, the reflectivities are not corrected for~~  
837 ~~attenuation, however, in Fig. 12, the attenuation-corrected reflectivities are plotted. Uncorrected-~~  
838 ~~reflectivities from Table 5, attenuations from Table 3, and Eq. 1 were used to calculate the~~  
839 ~~corrected reflectivities. Also shown is a subset of the S/Z pairs from PV11's Fig. 11 ( $0.01 < Z <$~~   
840  ~~$10 \text{ mm}^6 \text{ mm}^{-3}$ ) and the PV11 best-fit line (black). In the figure legend, results from PV11 are~~  
841 ~~specified as  $S(\rho_1)/Z$  because those authors applied the lower of two density size functions ( $\rho_1$ )~~  
842 ~~with airborne measurements of optical particle images to calculate the snowfall rates (Sect. 1).~~  
843 ~~Our data pairs plot above the  $S(\rho_1)/Z$  line but within the variability of PV11's measurements.~~

844 Our S/Z pairs are presented in Table 5 where the indexes ( $i=0$  and  $i=1$ ) are used to  
845 indicate results derived for the averaging intervals. In Table 5, reflectivities are not corrected for  
846 attenuation, however, in Fig. 12a, attenuation-corrected reflectivities are plotted. Reflectivities  
847 from Table 5, attenuations from Table 3, and Eq. 1 were used to calculate the corrected  
848 reflectivities. Also shown is a subset of the S/Z pairs from PV11's Fig. 11 ( $0.01 < Z < 10 \text{ mm}^6$   
849  $\text{mm}^{-3}$ ) and the PV11 best-fit line (black). Results from PV11 are specified as  $S(\rho_1)/Z$  because  
850 those authors applied the lower of two density-size functions ( $\rho_1$ ), and the lower of two fall  
851 speed-size functions, with airborne measurements, in calculations of snowfall rates (Sect. 1).

852

853

854



855

856

857

858

859

860

861

862

863

864

865

866

867

868

Figure 12— Snowfall rate versus radar reflectivity. Colored circles indicate attenuation-corrected reflectivities (Table 3, Table 5, and Eq. 1) for the  $i = 0$  and  $i = 1$  averaging intervals. The  $S(\rho_t)/Z$  points are a subset from PV11's Fig. 11 ( $0.01 < Z < 10 \text{ mm}^6 \text{ mm}^{-3}$ ). Also plotted is the PV11 best fit line (black), the  $S/Z$  relationship from Matrosov (2007), the  $S/Z$  relationship abbreviated SSKB (Sect. 1), and the swath of  $S/Z$  relationships, for crystals, from Hiley et al. (2011).

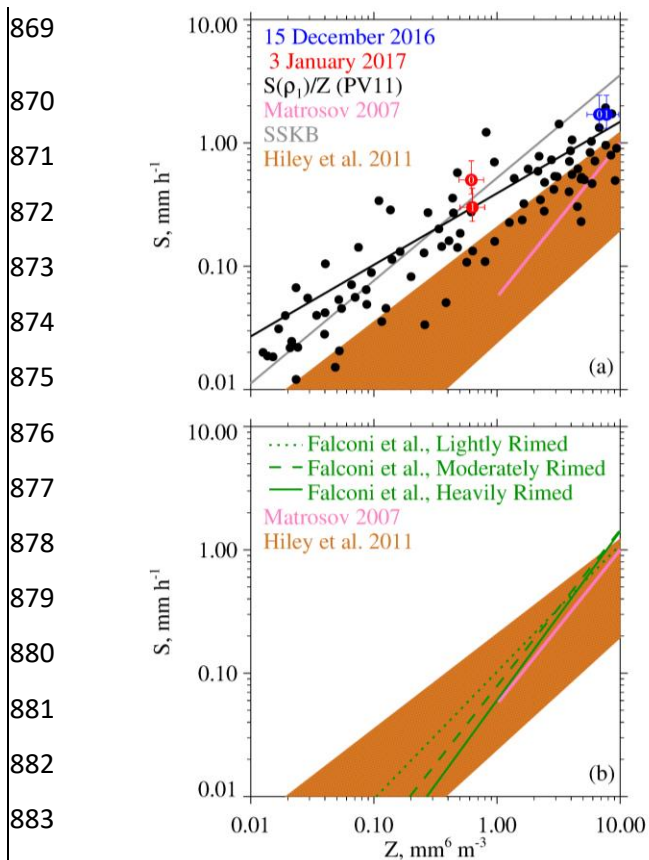


Figure 12 – a) Snowfall rate versus radar reflectivity. Colored circles indicate attenuation-corrected reflectivities (Table 3, Table 5, and Eq. 1) for the  $i = 0$  and  $i = 1$  averaging intervals. Error bars on these points represent the precision of the  $Z$  measurement (Sect. 2.3) and the precision of the  $S$  measurement (Sect. 2.4). The  $S(\rho_1)/Z$  points are a subset from PV11's Fig. 11 ( $0.01 < Z < 10 \text{ mm}^6 \text{ mm}^{-3}$ ). Also plotted is the PV11 best-fit line (black) (Sect. 1), the  $S/Z$  relationship from Matrosov (2007) (Sect. 1), the  $S/Z$  relationship abbreviated SSKB (Sect. 1), and the swath of  $S/Z$  relationships from Hiley et al. (2011) (Sect. 1). b)  $S/Z$  relationships from Falconi et al. (2018) (their Table 2) (Sect. 1), the Matrosov (2007) relationship, and the swath of  $S/Z$  relationships from Hiley et al. (2011) are shown.

896           There are two potential biases in the values of  $S$  we measured (Table 5) and plot (Fig.  
897 12a). First, the two snowfall events had flight-level vertical wind velocities that were positive  
898 (upward) upwind of the summit, and vice versa downwind of the summit. Except for the  
899 strongest downdraft on 3 January 2017, the magnitude of this variance is  $\sim 1 \text{ m s}^{-1}$  (Figs. 5b and  
900 5d). Assuming  $1 \text{ m s}^{-1}$  was the downward wind immediately over the hotplate, the snow particles  
901 would have approached the gauge faster than their fall speed. Our basis for stating this is fall  
902 speeds for the mode sizes discussed in Sect. 3.6 (1600 and  $400 \mu\text{m}$ ) and our assumption that the  
903 particles were graupel. (Table 6 has these characteristic sizes and fall speeds.) However, the  
904 conjectured downdraft speed is likely an overestimate - because of divergence occurring as the  
905 draft approached the surface - and because the sizes in Table 6 likely underestimate what fell to  
906 the hotplate. Relevant to the last of these assertions, we used the altitude/T/RH measurements  
907 (Table 2) to calculate the vertical distance available for growth via riming, and thus for a fall  
908 speed increase, between the flight level and the lifted condensation level. Assuming an  
909 adiabatically-stratified liquid cloud and unit collection efficiency (these assumptions  
910 overestimate growth by riming), and no change of particle crosssection (underestimates growth by  
911 riming), our calculations indicate that relative increases of size and fall speed were 40 and 20 %,  
912 respectively, on 3 January 2017, and that these relative increases were a factor-of-two larger on  
913 15 December 2016. ~~There are two potential biases in the values of  $S$  we tabulate (Table 5) and  
914 plot (Fig. 12). First, the two snowfall events had flight-level vertical wind velocities that were  
915 positive (upward) upwind of the summit, and vice versa downwind of the summit. Except for the  
916 strongest downdraft on 3 January 2017, the magnitude of this variance is  $\sim 1 \text{ m s}^{-1}$  (Figs. 5b and  
917 5d). Assuming  $1 \text{ m s}^{-1}$  was the downward wind immediately over the hotplate, the snow particles  
918 would have approached the gauge faster than their fall speed, and especially so on 3 January~~

919 ~~2017. Our basis for stating this is fall speeds for the mode sizes discussed in Sect. 3.6 (1600 and~~  
920 ~~400  $\mu\text{m}$ ) and our assumption that the particles were graupel. (Table 6 has these characteristic~~  
921 ~~sizes and fall speeds.) However, the conjectured downdraft speed is likely an overestimate—~~  
922 ~~because of divergence occurring as the draft approached the surface—and because the sizes in~~  
923 ~~Table 6 likely underestimate what fell to the hotplate. Relevant to the last of these assertions, we~~  
924 ~~used the T/RH/altitude measurements (Table 2) to calculate the vertical distance available for~~  
925 ~~growth via riming, and thus for a fall speed increase, between the flight level and the lifted~~  
926 ~~condensation level. Assuming an adiabatically stratified liquid cloud and unit collection~~  
927 ~~efficiency (these assumptions overestimate growth by riming), and no change of particle~~  
928 ~~cross-section (underestimates growth by riming), our calculations indicate that relative increases of~~  
929 ~~size and fall speed were 40 and 20 %, respectively, on 3 January 2017, and that these relative~~  
930 ~~increases were a factor of two larger on 15 December 2016.~~

931

932 Table 6 – Estimates of snow particle fall speed

Date	Mode Size, $\mu\text{m}$	Assumed Particle Type	Fall Speed, $\text{m s}^{-1}$	Reference
15 December 2015	1600	graupel	1.4	PV11; assuming $\rho_1$ in their Fig. <del>ure</del> 5
3 January 2016	400	graupel	0.7	PV11; assuming $\rho_1$ in their Fig. <del>ure</del> 5

933

934

935           Second, there is concern that values of  $S$  from 3 January 2017 are underestimated.  
936   Although values of  $S$  must be  $> 0$ , we presented 1 Hz values (gray points, Fig. 8) approaching -  
937    $0.3 \text{ mm h}^{-1}$ . Negative values resulted because we did not impose a threshold of  $0 \text{ mm h}^{-1}$  on the  
938   uncorrected snowfall rates (this thresholding is discussed in Z18) and because negative snowfall  
939   rate values (uncorrected for catch inefficiency) are amplified by the gauge-catch correction (Sect.  
940   2.4). The implication is that  $0.2 \text{ mm h}^{-1}$  could be added to the one-minute averaged values of  $S$  in  
941   Table 5 and in Fig. 12a. Here, the assumption is that an averaged  $S$  of  $-0.2 \text{ mm h}^{-1}$ , in Fig. 8, is  
942   indicating no snowfall at the hotplate; however, because the hotplate was operated autonomously  
943   (Sect. 2.1) we have no way to verify the assumption.

944           ~~Second, there is concern that values of  $S$  from 3 January 2017 are underestimated.~~  
945   ~~Although, values of  $S$  must be  $> 0$ , we presented 1 Hz values (gray points, Fig. 8) approaching -~~  
946    ~~$0.3 \text{ mm h}^{-1}$ . Negative values resulted because we did not impose a threshold of  $0 \text{ mm h}^{-1}$  on the~~  
947   ~~uncorrected snowfall rates (this thresholding is discussed in Z18) and because negative snowfall~~  
948   ~~rate values (uncorrected for catch inefficiency) are amplified by the gauge-catch correction (Sect.~~  
949   ~~2.4). The implication is that  $0.2 \text{ mm h}^{-1}$  could be added to the one minute averaged values of  $S$  in~~  
950   ~~Table 5 and in Fig. 12. Here, the assumption is that an averaged  $S$  of  $-0.2 \text{ mm h}^{-1}$ , in Fig. 8, is~~  
951   ~~indicating no snowfall at the hotplate; however, because the hotplate was operated autonomously~~  
952   ~~(Sect. 2.1) we have no way to verify the assumption.~~

953

954 **4 – Results**

955 Figure 12a shows the four S/Z pairs (red and blue circles, our measurements) after the  
956 reflectivities were corrected for attenuation. The error bars on these data pairs represent the  
957 precision of the Z measurement (Sect. 2.3) and the precision of the S measurement (Sect. 2.4).  
958 Presentation clarity was what guided the selection of S and Z axis ranges in this figure but with  
959 the consequence that 32 of PV11's S/Z pairs are not shown because they plot at  $Z > 10 \text{ mm}^6 \text{ m}^{-3}$ .  
960 The way that the PV11 data pairs scatter closest to  $Z = 10 \text{ mm}^6 \text{ m}^{-3}$ , combined with the fact that  
961 the PV11 data points at  $Z > 10 \text{ mm}^6 \text{ m}^{-3}$  are not shown, could lead to the interpretation that the  
962 slope describing the best-fit relationship at Z approximately  $> 2 \text{ mm}^6 \text{ m}^{-3}$  should be decreased  
963 relative to the slope of the PV11 best-fit line. Readers who view PV11's Fig. 11 will conclude  
964 that this interpretation is not warranted. The four S/Z pairs (red and blue circles) plot above the  
965 PV11 best-fit line but within the variability of PV11's S/Z pairs.

966 Computational S/Z relationship have inputs from parameterized descriptions of density,  
967 shape, fall speed, PSD, and particle size (Sect. 1). Matrosov (2007) did calculations for the snow  
968 particle type known as aggregates. Hiley et al. (2011) did calculations for 20 snow particle types.  
969 Except for a S/Z calculation done for aggregate snowflakes, the calculations of Hiley et al.  
970 (2011) were for the particle type known as vapor-grown crystals. Hiley et al. (2011) did not  
971 model spherical snow particles. The latter were modeled by Surussavadee and Staelin (2007) and  
972 Kulie and Bennartz (2009). In Fig. 12a, the abbreviation SSKB is used to symbolize the  
973 computational S/Z relationship for spherical snow particles.

974 Fig. 12a shows the separation between our S/Z pairs and the Matrosov (2007) calculation.  
975 The separation is about a factor of two for the points obtained on 15 December 2016. The points  
976 obtained on 3 January 2017 plot at a Z smaller than the lower-limit of the calculation. Since the



977 particle images (Fig. 11a-b) reveal no evidence for the particle type modeled by Matrosov (2007)  
978 (aggregate snowflakes), it is not surprising that the calculation is not representative of our  
979 measurements.

980 Departures between our S measurements (Fig. 12a) and S/Z calculations from Hiley et al.  
981 (2011) were evaluated as the vertical distance between the top of the orange region and our S/Z  
982 data pairs. Snowfall rates at the top of the orange region were calculated using attenuation-  
983 corrected reflectivities (Eq. 1 and Table 5) and using the upper-limit S/Z equation from Hiley et  
984 al. (2011) ( $S = 0.21 \cdot (Z')^{0.77}$ ; Sect. 1 and Eq. 1). The departures were evaluated as a relative  
985 difference expressed as  $(S_{HP} - S)/S$  with  $S_{HP}$  one of four snowfall rates from Table 5. The relative  
986 difference is no smaller than 0.7 and 1.0 on 15 December and 3 January, respectively. These  
987 minimum relative differences exceed the hotplate precision (Sect. 2.4) by at least a factor of two.  
988 It is concluded that our paired values of surface-measured precipitation rate and aircraft-  
989 measured radar reflectivity, after correcting for attenuation, provide evidence that a calculation  
990 of S based on the Hiley et al. (2011) upper-limit, when applied to rimed snow particles, is  
991 associated with a low-biased estimate of S.

992 A plausible explanation for the low bias is the smaller density implicit in most  
993 computationally-based S/Z relationships and especially those which assume that snow particles  
994 are crystals. Densities are quite different for crystals versus that for rimed snow particles. For  
995 example, in Brown and Francis (1995), assuming a 2 mm crystal, the density is  $\sim 30 \text{ kg m}^{-3}$ ,  
996 whereas in PV11 (their Eq. 1), assuming a 2 mm graupel particle, the density is  $\sim 200 \text{ kg m}^{-3}$ .  
997 Fig. 12a also has the SSKB relationship. This was developed using density =  $200 \text{ kg m}^{-3}$  (Sect. 1).

998 Compared to  $S/Z$  relationship represented by top of the orange region in Fig. 12a, the SSKB line  
999 plots closer to our data points and closer to many of those reported by PV11.

1000       Based on data from PV11 and our result, as well as the  $S/Z$  relationship abbreviated  
1001 SSKB (Sect. 1), it is expected that the  $S/Z$  relationships reported by Falconi et al. (2018) for  
1002 rimed snow particles (Sect. 1) would plot higher in  $S$ -versus- $Z$  space than illustrated in Fig. 12b.  
1003 Notably, only the upper-end of the Falconi et al. lines ( $Z > 8 \text{ mm}^6 \text{ m}^{-3}$ ) plot above the upper limit  
1004 that Hiley et al. (2011) established for unrimed snow particles. A plausible explanation for the  
1005 lower-than-expected  $S/Z$  relationships of Falconi et al. is now offered. Falconi et al. used liquid  
1006 water path as a proxy for the extent of snow particle riming (von Lerber et al. 2017). A  
1007 consequence may have been that the proxy did not dependably exclude unrimed snow particles  
1008 (crystals and aggregates) from the riming categories of Falconi et al. If this was true, then the  
1009 data groupings that were the basis for the Falconi et al.  $S/Z$  relationships may have been affected.  
1010 Further research is needed to resolve the reason for the mismatch between  $S/Z$  pairs, reported  
1011 both here and in PV11, and the  $S/Z$  relationships reported in Falconi et al.

1012       Our conclusion that the upper-limit  $S/Z$  relationship from Hiley et al. (2011)  
1013 underestimates  $S$  would be modified if our WCR-derived reflectivities were negatively biased.  
1014 Assuming the reflectivities are negatively biased by 2.5 dBZ, the minimum relative differences  
1015 discussed previously are no smaller than 0.1 and 0.3 on 15 December and 3 January,  
1016 respectively. A bias in reflectivity of this magnitude cannot be ruled out but neither can a  
1017 positive bias of the same magnitude (Sect. 2.3). The latter increases the minimum relative  
1018 differences to 1.6 and 2.2 on 15 December and 3 January, respectively. In each of these  
1019 calculations we have summed the attenuations (Table 3) with  $\pm 2.5$  dBZ and used Eq. 1 to  
1020 calculate error-perturbed reflectivities.

1021 The scatter of measurements in Fig. 12a, the plausibility of a -2.5 to +2.5 dBZ bias in  
1022 WCR reflectivity measurements, and error in measurement of S (Sect. 2.4), indicate that refined  
1023 techniques will be needed in future investigations which apply the approach described here.  
1024 Additionally, improved methods are needed to diagnose situations where riming is occurring  
1025 within clouds. Both lidars and radiometers can sense supercooled liquid water from space (e.g.,  
1026 Battaglia and Panegrossi, 2020), and if combined with Doppler radar, can diagnose precipitation  
1027 attributable to rimed snow particles. These approaches are being tested in ground-based field  
1028 studies (Kneifel et al. 2015; Moisseev et al. 2017; Mason et al. 2018) but are most reliable in  
1029 scenarios with the magnitude of vertical air speed smaller than particle fall speed.

1030 ~~Figure 12 shows our S/Z measurements after we corrected the reflectivities for~~  
1031 ~~attenuation. Below we compare our S/Z measurements to calculations reported by Hiley et al.~~  
1032 ~~(2011), but first, we consider the computational S/Z relationship reported by Matrosov (2007)~~  
1033 ~~and its relevance to our measurements. Since the particle images (Figs. 11a-b) reveal no~~  
1034 ~~compelling evidence for the aggregates modeled by Matrosov (2007), a model based on that~~  
1035 ~~particle type is not a useful comparator. Moreover, the overlap of PV11's S/Z measurements and~~  
1036 ~~Matrosov's S/Z calculations has already been discussed in the literature (PV11). However,~~  
1037 ~~before going forward, two clarifications will be made about PV11's data points in Fig. 12: 1)~~  
1038 ~~Presentation clarity was what guided our selection of the S and Z axis ranges in this figure but~~  
1039 ~~with the consequence that 32 of PV11's S/Z pairs are not shown at  $Z > 10 \text{ mm}^6 \text{ m}^{-3}$ . 2) The~~  
1040 ~~scatter of PV11 data at the largest values of Z in Fig. 12, combined with the fact that PV11~~  
1041 ~~points at  $Z > 10 \text{ mm}^6 \text{ m}^{-3}$  are not shown, could lead to the interpretation that the slope describing~~  
1042 ~~the relationship at Z approximately  $> 2 \text{ mm}^6 \text{ m}^{-3}$  should be decreased relative to the slope of the~~

1043 ~~PV11 best-fit line. Readers who view PV11's Fig. 11 will conclude that this interpretation is not~~  
1044 ~~warranted.~~

1045 ~~Calculated S/Z relationships have inputs from parameterized descriptions of density,~~  
1046 ~~shape, fall speed, and PSD. The analysis conducted by Hiley et al. (2011) is the most~~  
1047 ~~comprehensive in this regard, and except for the one aggregate particle type those authors~~  
1048 ~~considered, out of 20 total, they modeled ensembles of crystals. Additionally, Hiley et al. (2011)~~  
1049 ~~did not model ensembles of spherical snow particles. The latter were modeled by Surussavadee~~  
1050 ~~and Staelin (2007) and Kulie and Bennartz (2009), and in Fig. 12 we are using SSKB to~~  
1051 ~~symbolize that computational approach (Sect. 1).~~

1052 ~~Departures between our S measurements (Fig. 12) and S/Z calculations from Hiley et al.~~  
1053 ~~(2011) were evaluated as the vertical distance between the top of the orange region and our S/Z~~  
1054 ~~data points. Reflectivities at the top of the orange region were calculated using attenuation-~~  
1055 ~~corrected reflectivities (Eq. 1 and Table 5) and the upper-limit S/Z equation from Hiley et al.~~  
1056 ~~(2011) ( $S = 0.21 \cdot (Z^{\uparrow})^{0.77}$ ; Sect. 1). The departures were evaluated as a relative difference~~  
1057 ~~expressed as  $(S_{HP} - S)/S$  with  $S_{HP}$  one of four snowfall rates from Table 5. The relative difference~~  
1058 ~~is no smaller than 0.9 and 1.1 on 15 December and 3 January, respectively. These minimum~~  
1059 ~~relative differences exceed the hotplate precision (Sect. 2.4) by approximately a factor of three.~~  
1060 ~~We therefore conclude that our paired values of surface-measured precipitation rate and aircraft-~~  
1061 ~~measured radar reflectivity, after correcting for attenuation, provide evidence that a calculation~~  
1062 ~~of S based on the Hiley et al. (2011) upper limit, when applied to rimed snow particles, is~~  
1063 ~~associated with a low-biased estimate of S.~~

1064 A plausible explanation for the low bias is the smaller density implicit in most  
1065 computationally based S/Z relationships and especially those which assume that snow particles  
1066 are crystals. Densities are quite different for crystals versus that for rimed snow particles. For  
1067 example, in Kulie and Bennartz (2009; their Eq. 2), assuming a 2 mm crystal, the density is  $\sim 40$   
1068  $\text{kg m}^{-3}$ , whereas in PV11, assuming a 2 mm graupel particle, the density is  $\sim 200 \text{ kg m}^{-3}$ . Fig. 12  
1069 also has the SSKB relationship. This was developed using density =  $200 \text{ kg m}^{-3}$  (Sect. 1).  
1070 Compared to S/Z relationship represented by top of the orange region in Fig. 12, the SSKB line  
1071 plots closer to our data points and closer to most of those reported by PV11.

1072 Our conclusion that the upper limit S/Z relationship from Hiley et al. (2011)  
1073 underestimates S would be modified if the WCR derived reflectivities were negatively biased.  
1074 Assuming the reflectivities are negatively biased by 2.5 dBZ, the minimum relative differences  
1075 discussed previously are no smaller than 0.2 and 0.4 on 15 December and 3 January,  
1076 respectively. A negative bias of this magnitude cannot be ruled out but neither can a positive  
1077 bias of the same magnitude (Sect. 2.3). The latter increases the minimum relative differences to  
1078 1.9 and 2.3 on 15 December and 3 January, respectively.

1079 The scatter of measurements in Figure 12, and the plausibility of a  $-2.5$  to  $+2.5$  dBZ bias  
1080 in WCR reflectivity measurements, indicate that refined techniques will be needed for future  
1081 investigations. Additionally, improved methods are needed to diagnose situations where riming  
1082 is occurring within clouds. Both lidars and radiometers can sense supercooled liquid water from  
1083 space (e.g., Battaglia and Panegrossi, 2020), and if combined with Doppler radar, can diagnose  
1084 precipitation attributable to rimed snow particles. These approaches are being tested in ground-  
1085 based field studies (Kneifel et al. 2015; Moisseev et al. 2017; Mason et al. 2018).

1086

## 1087 5 - Conclusions

1088 ~~This study is significant because it brings together direct measurements of snowfall rate,~~  
1089 ~~measured at the ground, and measurements of reflectivity from an airborne W-band radar.~~  
1090 ~~As shown in Fig. 12, our observations do not depart strongly from the PV11 best-fit line;~~  
1091 ~~however, they do plot somewhat larger.~~

1092 The reported measurements consist of surface measurements of  $S$  and near-surface  
1093 measurements of  $Z$ . The latter came from overflights of a ground site, where a precipitation  
1094 gauge was operated, and were acquired using an airborne W-band radar. The values of  $Z$  were  
1095 corrected for attenuation. The reported  $S/Z$  pairs plot at or above the  $S$ -versus- $Z$  best-fit line of  
1096 PV11. However, the points do not depart beyond the variability evident in a replotting of  $S/Z$   
1097 pairs from PV11. The PV11 data came from airborne measurements of W-band reflectivity,  
1098 acquired within  $\pm 100$  m of flight level, and from coincident measurements of snow particle  
1099 imagery. PV11 used a density-size function and a fall speed-size function, and measurements  
1100 (PSD and particle images) to calculate  $S$ .

1101 There is an offset between the  $S$  points, reported here, and reflectivity-dependent  $S$  values  
1102 calculated at an upper-limit  $S/Z$  relationship for unrimed snow particles (Hiley et al. 2011). The  
1103 offset is larger than the precision of the  $S$  measurement. This suggests that a measured  $Z$  and the  
1104 Hiley et al. (2011) upper limit will produce an underestimate of precipitation in scenarios  
1105 dominated by rimed snow particles.

1106 New research is needed to refine the  $S/Z$  relationship for rimed snow particles. This could  
1107 be computational – e.g., investigating the utility of parameterizing  $S$  in terms of both  $Z$  and  
1108 density – or could be observational. Unlike the investigation of PV11, where only an airborne

1109 platform was employed, we have demonstrated that useful information can be obtained using  
1110 coordinated ground-based and airborne systems. Another approach would be with only ground-  
1111 based instrumentation. This would avoid some of the complications encountered in this study,  
1112 including W-band attenuation and a reliance on particle imagery acquired aloft. A study with  
1113 both ground-based and airborne systems would be useful for understanding a S/Z mismatch,  
1114 apparent at  $Z < 8 \text{ mm}^6 \text{ m}^{-3}$ , and which is larger than the offset summarized in the previous  
1115 paragraph. Elements of the mismatch are the S/Z measurements reported by PV11, the  
1116 measurements reported here, and the measurement-based S/Z relationships reported by Falconi et  
1117 al. (2018). These three research teams reported measurements relevant to the development of a  
1118 S/Z relationship for rimed snow particles. ~~This excess could be consistent with downslope flow  
1119 that occurs in lee of the Medicine Bow Mountains (Figs. 5a and 5d) or with calculations which  
1120 indicate that larger density is associated with larger S, in the S versus Z coordinate system  
1121 (PV11), combined with the intrinsic variability of rime ice (Macklin 1962).~~

1122 ~~If the downslope flow hypothesis is correct, and the PV11 best fit line is applied to  
1123 retrieve S in settings with rimed snow particles, we expect a negatively biased S retrieval  
1124 leeward of a ridgeline, and a positively biased retrieval windward of a ridgeline. This follows  
1125 because PV11 did not account for the effect of vertical air motion on their S/Z relationship,  
1126 because of how vertical air motion changes windward to leeward across the Medicine Bow  
1127 Mountain ridgeline (Figs. 5b-5d), and because the magnitudes of the windward/leeward vertical  
1128 winds are comparable to the downward speed of rimed snow particles in quiescent air. Analysis  
1129 of existing data, for example from the SNOWIE project that deployed in western Idaho in 2017  
1130 (Tessendorf et al. 2019), could further explore the hypothesis.~~

~~New research can also refine the S/Z relationship for rimed snow particles. This could be computational—exploring the utility of parameterizing S in terms of both Z and density—or could be observational. Unlike the investigation of PV11, where only an airborne platform was employed, we have demonstrated how useful information can be obtained with ground-based and airborne systems. Another approach would be with collocated ground-based instrumentation, for density and particle imaging, and for measuring wind, snowfall rate, and radar reflectivity. This would avoid some of the complications encountered in this study, including W-band attenuation and a reliance on particle imagery acquired aloft.~~

~~A close-range measuring radar might also allow retrievals closer to the surface than in this work. Improvement of methods that remotely sense supercooled cloud water are also needed.~~

## 6 - Appendix

This appendix explains how HP (hotplate) and WCR (Wyoming Cloud Radar) averages were evaluated. The scheme starts with an HP averaging interval (duration 60 s) and derives a WCR averaging interval and a WCR averaging domain. The latter encompasses a subset of the altitude-time cross-section sampled by the WCR. The top boundary of the domain was derived using vertical-component Doppler velocities within the interval/domain. Because of this dependence, the line defining the top boundary ~~had to be~~ **was** derived iteratively.

With the overflight time symbolized  $t_o$ , the beginning and ending times of the first of two 60-second HP averaging intervals are

$$t_{HP,B} = t_o \tag{A1}$$

$$t_{HP,E} = t_o + 60 \tag{A2}$$



1153 Since two adjacent HP averaging intervals are evaluated in this analysis, we express the  
 1154 averaging times with the following recursive equations

$$1155 \quad t_{HP,B}(i) = t_O + i \cdot 60 \quad (A3)$$

1156 and

$$1157 \quad t_{HP,E}(i) = t_O + (i+1) \cdot 60. \quad (A4)$$

1158 In Eqs. A3-A4 the index is  $i \in \{0, 1\}$ . A special case with  $i=2$  is also analyzed in Sect. 3.5,

1159 Analogous to the recursion in Eq. A4, the ending time of a WCR averaging interval is

$$1160 \quad t_{WCR,E}(i) = t_O - i \cdot 60 \cdot v_w / g_s. \quad (A5)$$

1161 Here  $v_w$  is a wind advection speed (discussed below) and the second term on the rhs is a wind  
 1162 advection distance divided by the WKA (Wyoming King Air) ground speed ( $g_s$ ). Analogous to  
 1163 the Eq. A5, the beginning time of a WCR averaging interval is

$$1164 \quad t_{WCR,B}(i) = t_{WCR,E} - (i+1) \cdot 60 \cdot v_w / g_s \quad (A6)$$

1165 The wind advection speed ( $v_w$ ) in Eqs. A5-A6 was calculated using an altitude-  
 1166 dependent west-to-east wind velocity ( $u$ ) and an altitude-dependent south-to-north wind  
 1167 velocity ( $v$ ). These altitude-dependent component velocities were calculated using the  
 1168 horizontal wind vectors in the penultimate and last columns of Table 2. Plots of the component  
 1169 velocities versus altitude and the linear functions used to relate component velocities to altitude  
 1170 are presented in Figs. A1a-b.

1171 An altitude ( $z' = 3400$  m) was assumed for evaluating the horizontal wind advection  
 1172 vector. This is the altitude of the ridges west and northwest of the HP site (Figs. 3a-b).

1173 The WKA track vector (Table 2) defines the vertical plane of the WCR measurements.  
 1174 We assumed that wind advection of snow particles occurred parallel to this vector. With the  
 1175 assumption stated in the previous paragraph, the horizontal wind advection speed ( $v_w$ ) was  
 1176 calculated as the projection of the horizontal wind vector onto the track vector.

$$1177 \quad v_w = \frac{u(z') \cdot gs_x + v(z') \cdot gs_y}{(gs_x^2 + gs_y^2)^{1/2}} \quad (A7)$$

1178 In Eq. A7 the west-to-east and south-to-north components of the track vector are symbolized  $gs_x$   
 1179 and  $gs_y$ . Vector representations of the track vector are in Table 2. On 14/15 December 2016 and  
 1180 3 January 2017, the values of  $v_w$  are 7.4 and 8.9 m s<sup>-1</sup>, respectively.

1181 In addition to the properties  $gs$  and  $v_w$  used to evaluate Eqs. A5-A6, a WCR averaging  
 1182 interval/domain was evaluated using a snow particle downward speed (Eq. A8).

$$1183 \quad v_p = |\langle V_D \rangle| + \sigma_{V_D} \quad (A8)$$

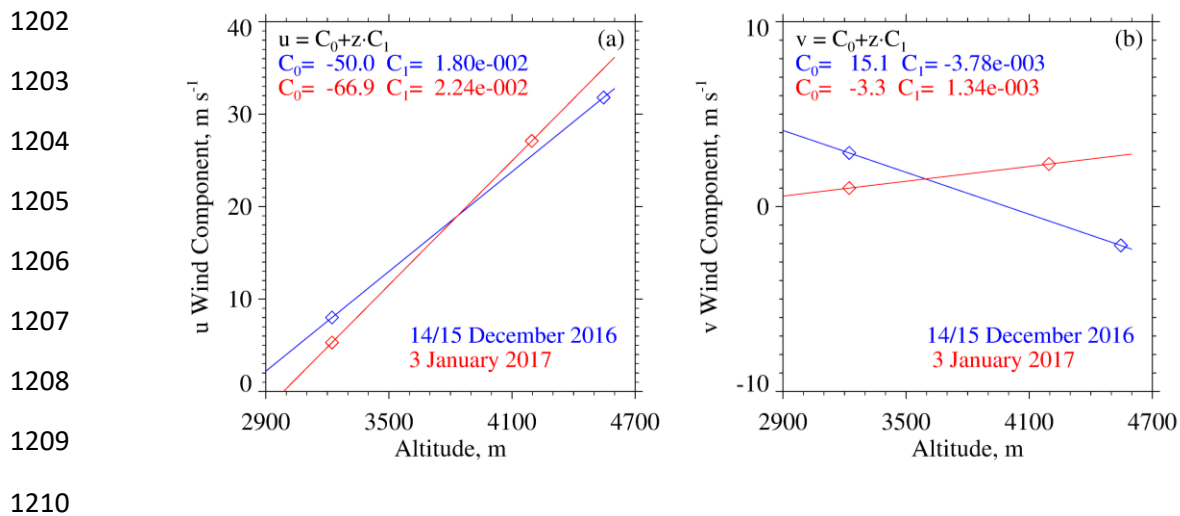
1184 Here,  $\langle V_D \rangle$  is the average of Doppler velocities within an averaging interval/domain,  $|\langle V_D \rangle|$   
 1185 is the absolute value of the average, and  $\sigma_{V_D}$  is the standard deviation of the average. On both  
 1186 the lhs and rhs of Eq. A8, all terms are greater than zero.

1187 We interpret  $v_p$  as the maximum likely snow particle speed toward the ground. There are  
 1188 three reasons for this: 1) For the WCR averaging intervals/domains we analyzed, values of  
 1189  $\langle V_D \rangle$  were consistently less than zero (Table 5). This indicates that snow particles (on average)  
 1190 were moving toward the ground. 2) Again, for the WCR averaging intervals/domains we  
 1191 analyzed,  $\sigma_{V_D}$  was comparable to  $|\langle V_D \rangle|$ . This indicates that turbulent eddies transported snow  
 1192 particles upward and downward at a speed comparable their downward speed in **quiescentstill**

1193 air. 3) The  $V_D$  are reflectivity weighted (Haimov and Rodi 2013) and are thus indicative of the  
1194 motion of the largest particles within an averaging interval/domain.

1195 We now focus on the top boundary of a WCR averaging interval/domain. Figures 6b and  
1196 6d have representations of the boundary. The slope defining this boundary was calculated as  
1197  $-v_p \cdot g_s / v_w$ . That is, particles below this boundary moved downward sufficiently fast and  
1198 horizontally sufficiently slow to advect reasonably close to the hotplate. Starting with diagnosed  
1199 values of  $g_s$  and  $v_w$ , the values of  $v_p$  and slope, were derived iteratively. The precision of the  
1200 derived  $v_p$  is  $\pm 0.1 \text{ m s}^{-1}$ .

1201



1211 Figure A1 – (a) West-to-east ( $u$ ) wind velocity derived using measurements from the WKA and  
 1212 the AmeriFlux (AF) tower. Also shown is the linear function used to relate  $u$  to altitude. (b)  
 1213 South-to-north ( $v$ ) wind velocity derived using measurements from the WKA and AF. Also  
 1214 shown is the linear function used to relate  $v$  to altitude. WKA and AF velocities are presented as  
 1215 vectors in the penultimate and last columns of Table 2.

1216

1217 Data Availability. The WKA and WCR measurements can be obtained from the SNOWIE data  
1218 archive of NCAR/EOL, which is sponsored by the National Science Foundation. Hotplate gauge  
1219 measurements are at <https://doi.org/10.15786/20103146>. The US-GLE AmeriFlux measurements  
1220 are at <https://ameriflux.lbl.gov/>. The Brooklyn Lake SNOTEL gauge measurements are at  
1221 <https://www.wcc.nrcs.usda.gov/snow/>. Merged Hotplate, SNOTEL, and AmeriFlux data  
1222 sequences from 14/15 December 2016 and 3 January 2017 are in Snider (2023).

1223

1224 Author contributions. JS and MB wrote the grant proposal that funded this research. Field  
1225 measurements were performed by SF, SM, SH, MB, and JS. SF wrote her MS dissertation, and  
1226 this was adapted for this paper by JS. KS processed the snow particle imagery. AM maintained  
1227 the measurement sites. All authors contributed to the editing of this paper.  
1228

1229 **Acknowledgements –**

1230 We acknowledge ~~the expert~~ technical assistance provided by David Plummer, Larry  
1231 Oolman, Zane Little, Brent Glover, Edward Sigel, Thomas Drew, and Brett Wadsworth. We  
1232 thank SNOWIE project PI Jeffery French, who provided the flight data, Gabor Vali who  
1233 provided the S/Z data points in Fig. ~~ure~~ 12a, and John Frank and John Korfmacher who acquired  
1234 the GLE-US AmeriFlux data set. This work was supported by the United States National Science  
1235 Foundation (Award Number 1850809) and the John P. Ellbogen Foundation.

1236

1237 **References**

- 1238 AmeriFlux, <https://ameriflux.lbl.gov/>, 2021
- 1239 Battaglia, A. and Panegrossi, G., What Can We Learn from the CloudSat Radiometric Mode Observations  
1240 of Snowfall over the Ice-Free Ocean?, 12, 3285, <https://doi.org/10.3390/rs12203285>, 2020
- 1241 Boudala, F.S., R. Rasmussen, G.A. Isaac, and B. Scott, Performance of Hot Plate for Measuring Solid  
1242 Precipitation in Complex Terrain during the 2010 Vancouver Winter Olympics, *J. Atmos. Oceanic  
1243 Technol.*, 31, 437–446, <https://doi.org/10.1175/JTECH-D-12-00247.1>, 2014
- 1244 Braham , R. R., Snow Particle Size Spectra in Lake Effect Snows. *J. Appl. Meteor. Climatol.*, 29, 200–207,  
1245 [https://doi.org/10.1175/1520-0450\(1990\)029<0200:SPSSIL>2.0.CO;2](https://doi.org/10.1175/1520-0450(1990)029<0200:SPSSIL>2.0.CO;2), 1990
- 1246 Brock, F. V., and Richardson, S. J., *Meteorological Measurement Systems*, Oxford University Press, New  
1247 York, 304 pp., 2001
- 1248 Brown, P. R. A., and P. N. Francis, Improved Measurements of the Ice Water Content in Cirrus Using a  
1249 Total-Water Probe. *J. Atmos. Oceanic Technol.*, 12, 410–414, [https://doi.org/10.1175/1520-  
1250 0426\(1995\)012<0410:IMOTIW>2.0.CO;2](https://doi.org/10.1175/1520-0426(1995)012<0410:IMOTIW>2.0.CO;2), 1995
- 1251 Cocks, S.B., S.M. Martinaitis, B. Kaney, J. Zhang, and K. Howard, MRMS QPE Performance during the  
1252 2013/14 Cool Season, *J. Hydrometeor.*, 17, 791–810, <https://doi.org/10.1175/JHM-D-15-0095.1>,  
1253 2016
- 1254 Faber, S., French, J. R., and Jackson, R., Laboratory and in-flight evaluation of measurement uncertainties  
1255 from a commercial Cloud Droplet Probe (CDP), *Atmos. Meas. Tech.*, 11, 3645–3659,  
1256 <https://doi.org/10.5194/amt-11-3645-2018>, 2018
- 1257 Falconi, M. T., von Lerber, A., Ori, D., Marzano, F. S., and Moisseev, D.: Snowfall retrieval at X, Ka and  
1258 W bands: consistency of backscattering and microphysical properties using BAECC ground-based  
1259 measurements, *Atmos. Meas. Tech.*, 11, 3059–3079, <https://doi.org/10.5194/amt-11-3059-2018>,  
1260 2018
- 1261 Field, P.R., Hogan, R.J., Brown, P.R.A., Illingworth, A.J., Choullarton, T.W. and Cotton, R.J.,  
1262 Parametrization of ice-particle size distributions for mid-latitude stratiform cloud. *Q.J.R. Meteorol.  
1263 Soc.*, 131: 1997-2017. <https://doi.org/10.1256/qj.04.134>, 2005
- 1264 Fuller, S.E., Improvement of the Snowfall / Reflectivity Relationship for W-band Radars, MS Thesis,  
1265 Department of Atmospheric Science, University of Wyoming, 2020



- 1266 Geerts, B., Q. Miao, Y. Yang, R. Rasmussen, and D. Breed, An Airborne Profiling Radar Study of the  
1267 Impact of Glaciogenic Cloud Seeding on Snowfall from Winter Orographic Clouds, *J. Atmos. Sci.*,  
1268 67, 3286–3302, <https://doi.org/10.1175/2010JAS3496.1>, 2010
- 1269 Haimov, S., and Rodi, A., Fixed-Antenna Pointing-Angle Calibration of Airborne Doppler Cloud Radar,  
1270 *Journal of Atmospheric and Oceanic Technology*, 30, 2320-2335, <https://doi.org/10.1175/JTECH->  
1271 D-12-00262.1, 2013
- 1272 Hiley, M. J., M. S. Kulie, and R. Bennartz, Uncertainty Analysis for CloudSat Snowfall Retrievals, *J. Appl.*  
1273 *Meteor. Climatol.*, 50, 399–418, 2011
- 1274 Kneifel, S., von Lerber, A., Tiira, J., Moisseev, D., Kollias, P., and Leinonen, J., Observed relations between  
1275 snowfall microphysics and triple-frequency radar measurements. *J. Geophys. Res. Atmos.*, 120,  
1276 6034– 6055, doi: 10.1002/2015JD023156, 2015
- 1277 Kochendorfer, J., Nitu, R., Wolff, M., Mekis, E., Rasmussen, R., Baker, B., and Jachcik, A, Testing and  
1278 development of transfer functions for weighing precipitation gauges in WMO-SPICE, *Hydrology*  
1279 *and Earth System Sciences*, 2, 1437-1452, <https://doi.org/10.5194/hess-22-1437-2018>, 2018
- 1280 Korolev, A. V., E. F. Emery, J. W. Strapp, S. G. Cober, G. A. Isaac, M. Wasey, and D. Marcotte, Small ice  
1281 particles in tropospheric clouds: Fact or artifact? Airborne Icing Instrumentation Evaluation  
1282 Experiment, *Bull. Amer. Meteor. Soc.*, 92, 967–973, <https://doi.org/10.1175/2010BAMS3141.1>,  
1283 2011
- 1284 Kulie, M. S., and R. Bennartz, Utilizing Spaceborne Radars to Retrieve Dry Snowfall, *J. Appl. Meteor.*  
1285 *Climatol.*, 48, 2564–2580, <https://doi.org/10.1175/2009JAMC2193.1>, 2009
- 1286 Kulie, M. S., Milani, L., Wood, N. B., Tushaus, S. A., Bennartz, R., and L'Ecuyer, T. S., A Shallow  
1287 Cumuliform Snowfall Census Using Spaceborne Radar, *Journal of Hydrometeorology*, 4, 1261-  
1288 1279, <https://doi.org/10.1175/JHM-D-15-0123.1>, 2016
- 1289 Lawson, R. P., O'Connor, D., Zmarzly, P., Weaver, K., Baker, B., Mo, Q., and Jonsson, H., The 2D-S  
1290 (Stereo) Probe: Design and Preliminary Tests of a New Airborne, High-Speed, High-Resolution  
1291 Particle Imaging Probe, *J. Atmos. Ocean. Tech.*, 23, 1462–1477,  
1292 <https://doi.org/10.1175/JTECH1927.1>, 2006
- 1293 Liebe, H.J., Manabe, T., and Hufford, G.A., Millimeter-wave attenuation and delay rates due fog/cloud  
1294 conditions, *IEEE Trans. Antenn. Propag.*, 37, 1617–1623, 1989

- 1295 Liu, C.-L., and A. J. Illingworth, Toward more accurate retrievals of ice water content from radar  
1296 measurements of clouds, *J. Appl. Meteor.*, 39, 1130–1146, 2000
- 1297 Locatelli, J.D. and Hobbs, P.V., Fall speed and masses of solid precipitation particles, *J. Geophys. Res.*, 79,  
1298 2185–2197, <https://doi.org/10.1029/JC079i015p02185>, 1974
- 1299 Macklin, W.C., The density and structure of ice formed by accretion, *Q.J.R.Meteorol.Soc.*, 88: 30-50.  
1300 doi:10.1002/qj.49708837504, <https://doi.org/10.1002/qj.49708837504>, 1962
- 1301 ~~Marlow, S.A., J.M. Frank, M. Burkhart, B. Borkhuu, S.E. Fuller, and J.R. Snider, Snowfall measurements~~  
1302 ~~in mountainous terrain, in revision for the Journal of Applied Meteorology and Climatology,~~  
1303 ~~[http://www.das.uwyo.edu/~jsnider/JAMC-D-22-0093\\_6.pdf](http://www.das.uwyo.edu/~jsnider/JAMC-D-22-0093_6.pdf), 2023~~
- 1304 Marlow, S.A., J.M. Frank, M. Burkhart, B. Borkhuu, S.E. Fuller, and J.R. Snider, Snowfall Measurements  
1305 at Wind-exposed and Sheltered Sites in the Rocky Mountains of Southeastern Wyoming, in  
1306 revision for the Journal of Applied Meteorology and Climatology, [http://www-](http://www-das.uwyo.edu/~jsnider/manuscript_revision2.docx)  
1307 [das.uwyo.edu/~jsnider/manuscript\\_revision2.docx](http://www-das.uwyo.edu/~jsnider/manuscript_revision2.docx), 2023
- 1308 Martinaitis, S.M., S.B. Cocks, Y. Qi, B.T. Kaney, J. Zhang, and K. Howard, Understanding winter  
1309 precipitation impacts on automated gauge observations within a real-rime system, *J. Hydrometeor.*,  
1310 16, 2345-2363, <https://doi.org/10.1175/JHM-D-15-0020.1>, 2015
- 1311 Mason, S. L., Chiu, C. J., Hogan, R. J., Moisseev, D., and Kneifel, S., Retrievals of riming and snow density  
1312 from vertically pointing Doppler radars, *Journal of Geophysical Research: Atmospheres*, 123,  
1313 13,807– 13,834, <https://doi.org/10.1029/2018JD028603>, 2018
- 1314 Matrosov, S.Y., Modeling Backscatter Properties of Snowfall at Millimeter Wavelengths, *J. Atmos. Sci.*,  
1315 64, 1727-1736, <https://doi.org/10.1175/JAS3904.1>, 2007
- 1316 Moisseev, D., von Lerber, A., and Tiira, J., Quantifying the effect of riming on snowfall using ground-  
1317 based observations, *J. Geophys. Res. Atmos.*, 122, 4019–4037, doi:10.1002/2016JD026272, 2017
- 1318 Nemarich, J., Wellman, R.J., and Lacombe, J., Backscatter and attenuation by falling snow and rain at 96,  
1319 140, and 225 GHz, *IEEE Trans. Geosci. Remote*, 26, 319–329, 1988
- 1320 Panofsky, H.A. and Dutton, J.A., *Atmospheric Turbulence*, Wiley-Interscience, New York, 397 pp., 1984
- 1321 Pokharel, B. and G. Vali, Evaluation of Collocated Measurements of Radar Reflectivity and Particle Sizes  
1322 in Ice Clouds, *J. Appl. Meteor. Climatol.*, 50, 2104–2119, [https://doi.org/10.1175/JAMC-D-](https://doi.org/10.1175/JAMC-D-1005010.1)  
1323 [1005010.1](https://doi.org/10.1175/JAMC-D-1005010.1), 2011

- 1324 Rasmussen, R.M., J. Hallett, R. Purcell, S.D. Landolt, and J. Cole, The Hotplate precipitation gauge, J.  
1325 Atmos. Oceanic Technol., 28, 148-164, <https://doi.org/10.1175/2010JTECHA1375.1>, 2011
- 1326 R.M. Young Company, Model 05103 Wind Monitor, 2001
- 1327 ~~Serreze, M. C., M. P. Clark, and R. L. Armstrong, D. A. MacGinnis, and R. S. Pulwarty, Characteristics of~~  
1328 ~~the western United States snowpack from snowpack telemetry (SNOTEL) data, Water Resources~~  
1329 ~~Research, 35, 2145–2160, <https://doi.org/10.1029/1999WR900090>, 1999~~
- 1330 Skofronick-Jackson, G., and Coauthors, The Global Precipitation Measurement (GPM) Mission for  
1331 science and society, Bull. Amer. Meteor. Soc., 98, 1679–1695, [https://doi.org/10.1175/BAMS-D-](https://doi.org/10.1175/BAMS-D-15-00306.1)  
1332 [15-00306.1](https://doi.org/10.1175/BAMS-D-15-00306.1), 2017
- 1333 Smith, P.L., Equivalent radar reflectivity factors for snow and ice particles, J. Climatol. Appl. Meteor., 23,  
1334 1258–1260, [https://doi.org/10.1175/1520-0450\(1984\)023<1258:ERRFFS>2.0.CO;2](https://doi.org/10.1175/1520-0450(1984)023<1258:ERRFFS>2.0.CO;2), 1984
- 1335 Snider, J.R., Supplemental dataset for Marlow et al. (2023), <https://doi.org/10.15786/20247870>, 2023
- 1336 Surussavadee, C., and D. H. Staelin, Millimeter-Wave Precipitation Retrievals and Observed-versus-  
1337 Simulated Radiance Distributions: Sensitivity to Assumptions. J. Atmos. Sci., 64, 3808–3826,  
1338 <https://doi.org/10.1175/2006JAS2045.1>, 2007
- 1339 Tessendorf, S. A., and Coauthors, A transformational approach to winter orographic weather modification  
1340 research: The SNOWIE Project, Bulletin of the American Meteorological Society, 100, 71–92,  
1341 <https://doi.org/10.1175/BAMS-D-17-0152.1>, 2019
- 1342 Ulaby, F.T., Moore, R.K., and Fung, K., Microwave Remote Sensing: ~~Active and Passive, :-Active and~~  
1343 ~~Passive, Vol. 12, Microwave Remote Sensing Fundamentals and Radiometry, ARTECH HOUSE~~  
1344 ~~Inc. Addison-Wesley, Advanced Book Program, Norwood Reading, MA, p. 456., 1981~~
- 1345 ~~Vaisala, User's Guide, Vaisala Weather Transmitter, WXT520, 2012~~
- 1346 Vali, G. and Haimov, S., Observed extinction by clouds at 95 GHz, IEEE Trans. Geosci. Remote, 39, 190–  
1347 193, 2001
- 1348 von Lerber, A., D. Moisseev, L. F. Bliven, W. Petersen, A. Harri, and V. Chandrasekar: Microphysical  
1349 Properties of Snow and Their Link to Ze–S Relations during BAECC 2014. J. Appl. Meteor.  
1350 Climatol., 56, 1561–1582, <https://doi.org/10.1175/JAMC-D-16-0379.1>, 2017
- 1351 Wang, P.K., and W. Ji, Collision Efficiencies of Ice Crystals at Low–Intermediate Reynolds Numbers  
1352 Colliding with Supercooled Cloud Droplets: A Numerical Study, Journal of the Atmospheric

- 1353 Sciences, 57, 1001-1009, [https://doi.org/10.1175/1520-0469\(2000\)057<1001:CEOICA>2.0.CO;2](https://doi.org/10.1175/1520-0469(2000)057<1001:CEOICA>2.0.CO;2),  
1354 2000
- 1355 Wilson, J., and E. Brandes, Radar measurement of rainfall—A summary, *Bull. Amer. Meteor. Soc.*, 60,  
1356 1048–1058, [https://doi.org/10.1175/1520-0477\(1979\)060<1048:RMORS>2.0.CO;2](https://doi.org/10.1175/1520-0477(1979)060<1048:RMORS>2.0.CO;2), 1979
- 1357 Wolfe, J.P., and J.R. Snider, A relationship between reflectivity and snow rate for a high-altitude S-band  
1358 radar, *J. Appl. Meteor. Climatol.*, 51, 1111–1128, <https://doi.org/10.1175/JAMC-D-11-0112.1>,  
1359 2012
- 1360 ~~Young, H.D., *Statistical Treatment of Experimental Data*, pp. 172, McGraw Hill, New York, 1962~~
- 1361 Zaremba, T.J., and Coauthors, Vertical motions in orographic cloud systems over the Payette River Basin.  
1362 Part 1: Recovery of vertical motions and their uncertainty from airborne Doppler radial Velocity  
1363 Measurements, in press at the *Journal of Applied Meteorology and Climatology*,  
1364 <https://doi.org/10.1175/JAMC-D-21-0228.1>, 2022
- 1365 Zelasko, N., Wettlaufer, A., Borkhuu, B., Burkhart, M., Campbell, L. S., Steenburgh, W. J., and Snider,  
1366 J.R., Hotplate precipitation gauge calibrations and field measurements, *Atmos. Meas. Tech.*, 11,  
1367 441-458, <https://doi.org/10.5194/amt-11-441-2018>, 2018
- 1368 Zikmunda, J. and Vali, G., Fall patterns and fall velocities of rimed ice crystals, *J. Atmos. Sci.*, 29, 1334–  
1369 1347, [https://doi.org/10.1175/1520-0469\(1972\)029<1334:FPAFVO>2.0.CO;2](https://doi.org/10.1175/1520-0469(1972)029<1334:FPAFVO>2.0.CO;2), 1972

1370 Table 3—Attenuating component concentration, one-way pathlength, and summed two-way attenuation

Date	Cone. Vapor, kg·m <sup>-3</sup>	Cone. Cloud Water, kg·m <sup>-3</sup>	Cone. Snow Particles, kg·m <sup>-3</sup>	Pathlength Vapor, km	Pathlength Cloud Water, km	Overall Two- way Attenuation, dB
15 December 2016	2.7x10 <sup>-3</sup>	0.01x10 <sup>-3</sup>	0.10x10 <sup>-3</sup>	1.54	1.09	0.82 <sup>a</sup>
3 January 2017	1.8x10 <sup>-3</sup>	0.08x10 <sup>-3</sup>	0.05x10 <sup>-3</sup>	1.19	0.59	0.82 <sup>b</sup>

1371

1372 <sup>a</sup>—One-way attenuation coefficients are 0.14 dB/km for vapor (Ulaby et al. 1981), 0.052 dB/km for cloud

1373 water (Liebe et al. 1989; Vali and Haimov 2001), and 0.085 dB/km for snow particles (Nemariich

1374 et. al 1988).

1375

1376 <sup>b</sup>—One-way attenuation coefficients are 0.073 dB/km for vapor (Ulaby et al. 1981), 0.45 dB/km for cloud

1377 water (Liebe et al. 1989; Vali and Haimov 2001), and 0.045 dB/km for snow particles (Nemariich

1378 et. al 1988).

1379

|